CHRISTIAN-ALBRECHTS-UNIVERSITÄT ZU KIEL

MASTER'S THESIS

Mesoscale and submesoscale dynamics in the Caribbean Sea

Author:
Élise BEAUDIN
11113732

Supervisor:
Prof. Dr. Arne BIASTOCH

Co-supervisor:
Prof. Dr. Nadia PINARDI

A thesis submitted in fulfillment of the requirements for the degree of MSc: Climate Physics

in the

Theory and Modelling research group
GEOMAR - Helmholtz-Zentrum für Ozeanforschung Kiel

February 5, 2019

"Big whirls have little whirls that feed on their velocity, And little whirls have lesser whirls and so on to viscosity."

Lewis F. Richardson, 1922

CHRISTIAN-ALBRECHTS-UNIVERSITÄT ZU KIEL

Abstract

Mathematisch- Naturwissenschaftliche Fakultät
GEOMAR - Helmholtz-Zentrum für Ozeanforschung Kiel

MSc: Climate Physics

Mesoscale and submesoscale dynamics in the Caribbean Sea

by Élise BEAUDIN

Submesoscale processes are characterized by spatial scales of 1-10 km and timescales of hours to days. Observational data and high spatial resolution ocean modeling have recently exposed and confirmed the presence of these rich structures in the upper ocean. They play a crucial role in mixed-layer restratification and vertical transport of ocean tracers, therefore being substantial for mixing and biogeochemical processes. This thesis aims to study the submesoscale dynamics in the Caribbean Sea using high (1/32°, 3.5 km) and very-high (1/96°, 1.2 km) resolution models. The simulations were carried out using SURF (Trotta et al., 2016), a NEMO-based relocatable ocean modeling platform for downscaling, with GOFS16 (1/16°, 6.8 km) as initial and boundary conditions. The focus was put on a two-weeks period in February 2017, where a large anticyclonic eddy was found propagating westward in the northwest part of the basin. Research in this thesis includes a description of the mesoscale dynamics in the Caribbean Sea during the chosen time period with the GOFS16 model, which was found to compare nicely with observations from CTD and satellite data. The present study demonstrated that the development of submesoscale motions in the Caribbean sea was made possible, with a transition on a time-scale of days, at a horizontal resolution of 3.5 km. Submesoscale structures included thinner filaments and small-scale eddies ($\sim$ 10 km) of large Rossby number. The steepening of the kinetic energy spectra slopes with depth confirmed that the submesoscale motions were concentrated in the upper-oceanic layer, where restratification of the upper mixed-layer has been observed. The presence of submesoscale processes in the domain led to subsiding of the anticyclonic eddy. Frontogenesis and topographic wakes were the main mechanisms for the generation of submesoscale dynamics.

Zusammenfassung

Submesoskale Prozesse sind durch räumliche Skalen von 1-10 km und Zeitskalen von Stunden bis Tagen gekennzeichnet. Beobachtungsdaten und Modellierungen der Ozeane mit hoher räumlicher Auflösung haben kürzlich gezeigt, dass diese Strukturen im oberen Ozean vorhanden sind. Sie spielen eine entscheidende Rolle bei der Restratifizierung des Mixed-layers und beim vertikalen Transport von Tracern, weshalb sie für Vermischungsprozesse und biogeochemische Prozesse von erheblicher Bedeutung sind. Diese Thesis zielt darauf ab, die submesoskale Dynamik im Karibischen Meer anhand von Modellen mit hoher Auflösung (1/32°) und sehr hoher Auflösung (1/96°) zu untersuchen. Die Simulationen werden mit SURF (Trotta et al., 2016) durchgeführt, einer auf NEMO basierenden Plattform zur Ozeanmodellierung für das Downscaling mit GOFS16 als Anfangs- und Randbedingung. Der Fokus liegt auf einer zweiwöchigen Periode im Februar 2017, in der ein großer antizyklonischer Wirbel (*Eddy*) gefunden wurde, der sich im Nordwesten des Beckens nach Westen ausbreitet. Diese Thesis enthält eine Beschreibung der mesoskalen Dynamik im Karibischen Meer während des gewählten Zeitraums mit dem GOFS16-Modell, das sich gut mit Beobachtungen aus CTD- und Satellitendaten vergleichen lässt. Die Simulationen bei einer Auflösung von 3,5 km zeigten, dass eine Erhöhung der horizontalen Auflösung die Entstehung von ageostrophischen submesoskalen Merkmalen mit sich bringt, die die Restratifizierung des Mixed-layers verursachen und den mesoskalen Fluss beeinflussen. Dabei entstehen zusätzliche kleinskaligere Strukturen in den ozeanischen Tracern und den dynamischen Feldern, z.B. dünnere Filamente, die mit der kleinskaligen Frontogenese einher gehen. Die Oberflächendynamik umfasst kleinere Wirbel ($\sim$ 10 km) mit großer Rossby-Zahl, was die starke Ageostrophie submesoskaler Bewegungen unterstreicht. Die Verstärkung der submesoskalen Merkmale geschieht hauptsächlich in der oberen Schicht, was durch die zunehmende Steigung der Neigungen der kinetischen Energiespektren mit der Tiefe bestätigt wird. Am Rand des antizyklonischen Wirbels, in dem die ageostrophischen Bewegungen hauptsächlich auftreten, findet sich eine starke Restratifizierung innerhalb der Mixed-layer in Zeitskalen von Tagen. Die Erhöhung der horizontalen Auflösung führte zum Absinken des Zentrums des antizyklonischen Wirbels.

Acknowledgements

I would like to start with thanking my supervisor Nadia Pinardi, who generously hosted me at the University of Bologna and provided me with great support to make this thesis happen, along with the possibility of accomplishing amazing projects on the side. Thanks to Dr. Francesco Trotta for his availability and his support regarding numerical and scientific knowledge, and letting me use his creation SURF for the numerical simulations.

Thanks to my colleagues and friends Augusto, Kanwal and Giovanni for sharing the office, as well as their philosophical point of view and making my stay in Bologna unforgettable.

Thanks to my supervisor Arne Biastoch whose support, expertise and directives along the thesis greatly helped, and thanks to René whose contributions (especially for the kinetic energy spectrum) and comments helped my understanding of the topic. Thanks to Jannis for helping me with the german translation.

Thanks to my beloved friends Katt, Laura and Waithira with whom I shared these two years in Kiel and whose friendship and solidarity made me grow as a person and a woman. Thanks to my flatmates and friends Dario and Matteo, who supported me and taught me the Italian way of life.

Thanks to Iolande, Francine, Nadia and my mother Anne, women leaders and pioneers who keep inspiring me.

Thanks to my mother Anne, my father Éric, my brother Laurent, my cousin David, and all my family and friends for their love and encouragement through this process.

Declaration of Authorship

I, Élise BEAUDIN (Matrikelnr: 11113732), declare that this thesis titled "Mesoscale and submesoscale dynamics in the Caribbean Sea" and the work presented in it are my own. I confirm that this work was done wholly or mainly while in candidature for a research degree at this University, and that any part of this thesis has not previously been submitted for a degree or any other qualification at this University or any other institution. It is always clearly attributed where I have consulted the published work of others. The source where I have quoted from the work of others is always given. With the exception of such quotations, this thesis is entirely my own work. I have acknowledged all main sources of help and I have made clear exactly what was done by others and what I have contributed myself.

Erklärung
Hiermit erkläre ich, Élise BEAUDIN (Matrikelnr: 11113732) dass ich die vorliegende Arbeit "Mesoscale and submesoscale dynamics in the Caribbean Sea", selbständig und ohne fremde Hilfe angefertigt und keine anderen als die angegebenen Quellen und Hilfsmittel verwendet habe. Die eingereichte schriftliche Fassung der Arbeit entspricht der auf dem elektronischen Speichermedium. Weiterhin versichere ich, dass diese Arbeit noch nicht als Abschlussarbeit an anderer Stelle vorgelegen hat. (Name der Datei: MasterArbeit_Beaudin11113732.pdf).

Signed:

Date: 06.02.2019

Contents

Chapter 1

Introduction

The ocean circulation arises from the combination of a thermohaline component, and a wind-driven component. The thermohaline part is associated with heat fluxes and change in the salinity due to evaporation, precipitation and runoff, whereas the wind drives the near-surface frictional layer, initiating waves, inertial currents and Langmuir cells (Talley et al., 2011). Oceanic flows are, by nature, turbulent. These turbulence, which occur on many space and time-scales cause the flow to fluctuate in space and time. Turbulence arises from instabilities in the flow, which tend to occur when inertial forces become larger than other forces in the momentum balance (Olbers, Willebrand, and Eden, 2012). The physical oceanography processes that contribute to the ocean circulation variability, or turbulence, can be observed on a very wide range of spatial and temporal scales, spanning from molecular processes $\mathcal{O}$(1 mm) to the large-scale circulation $\mathcal{O}$(>1000 km). In the current context, the ocean dynamics is broken down into three spatial scales: the large-scale, the mesoscale and the submesoscale.

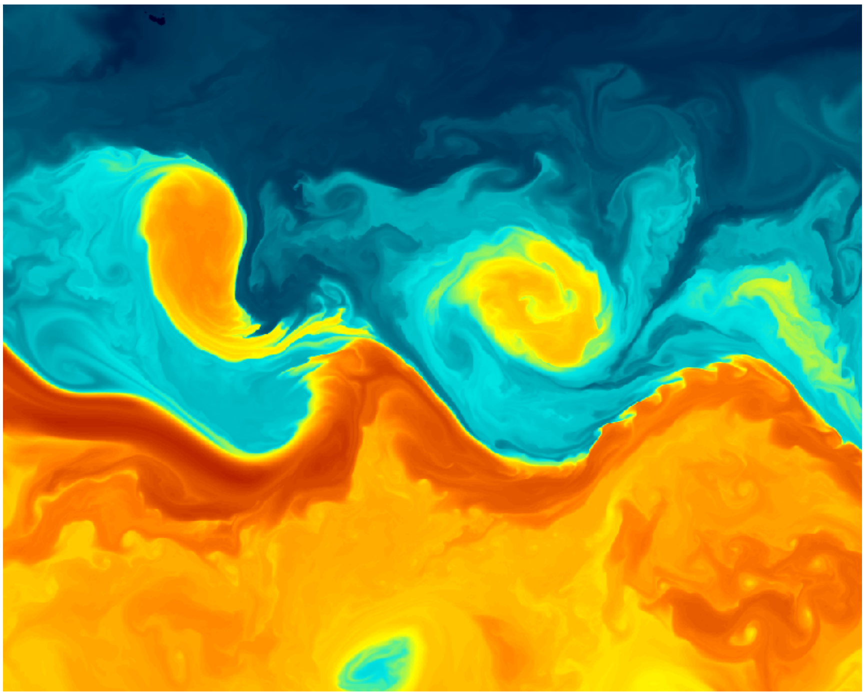

FIGURE 1.1: Submesoscale dynamics seen from sea-surface temperature with 500 m simulation over the Gulf Stream. (Gula et al., 2014)

The large-scale motions are embedded within immense gyres spanning several thousands of kilometers, driven by the wind-driven and thermohaline circulation, going clockwise in the northern hemisphere and anticlockwise in the southern hemisphere. The water flows for about ten years around the gyres and hundreds of years through the full ocean. The turbulent motion of the large-scale flows leads to the mesoscale dynamics, dominated by eddies and strong ocean currents such as the Gulf Stream. The horizontal length scales are kilometers to hundreds of kilometers, and time scales are weeks to months, sometimes years. These scales are associated to planetary waves such as Rossby and Kelvin waves. Mesoscale turbulence, mainly led by fronts and baroclinic instabilities within the mesoscale eddy field, yields the submesoscale motions.

Submesoscale processes are characterized by a horizontal spatial scale of 1-10 kilometers, and occur on a time scale of several hours to several days. They are correlated with a loss of geostrophic balance and take the shape of smaller eddies or narrow filaments (Fig.1.1). Their importance is highlighted in the restratification of the upper ocean and in enhancing the vertical velocities and small scale turbulence through the relative vorticity. They consequently play a role in the general circulation, but also at smaller scale, regarding mixing and transport of biogeochemical tracers. For example, they generate relatively strong vertical motions in the upper ocean, that exchange gases with the atmosphere. This mechanism acts as a pump that supplies nutrients to phytoplanktons and the euphotic zone (Lévy et al., 2012).

Numerical modeling in ocean science has brought major advances in understanding of the ocean and its interactions with the atmosphere (Talley et al., 2011). Ocean general circulation models solve dynamical equations using numerical methods along with approximations which depend on the resolved scale. The first three-dimensional ocean model was developed in the 1960s at the NOAA Geophysical Fluid Dynamics Laboratory and then available computational resources had it resolve horizontal scales of hundreds of kilometers. Simplifications to the physics and limited domain sizes allowed, in the 1970s, the resolution of mesoscale eddies of tens of kilometers, helping in understanding their interaction with the large-scale circulation. Until the early 2000s, the coarse grid resolution could not permit submesoscale processes. Simulations carried out with increased grid resolution, combined with high resolution resolution surface satellite images and following *in situ* measurements started revealing the rich and turbulent structure of the submesoscale fronts and instabilities, occurring widely in the upper ocean (Capet et al., 2008a).

In this thesis, a high and very-high resolution model is used in order to understand what are the features emerging while transitioning from a mesoscale to submesoscale-permitting horizontal grid, in the specific case of the Caribbean Sea. the dominant mechanisms for generation of submesoscale dynamics are investigated in ocean fronts occurring at the rim of an anticyclonic eddy, in the time-period of February 2017.

The following sections focus on describing the passage from large-scale to mesoscale, to submesoscale regimes, and point out the characteristics specific to each scales along with the underlying theory.

1.1 Theory and previous studies

The ocean currents are forced by heat, salt and momentum fluxes. Kinetic energy is transferred through the different scales in order to keep a climatic dynamical balance, from large-scale to small-scale motions following a dynamical route (see Fig.1.2) to dissipation. The passage from the balanced geostrophic motion to smaller unbalanced motions is done through different routes, such as energy loss at the bottom boundary layers (BBLs), spontaneously emitted internal gravity waves (IGWs) by eddies, or other processes that break the momentum-balance constraints and permit a forward energy cascade towards smaller scales (McWilliams, 2016). Submesoscale dynamics acts as a major conduit to dissipation.

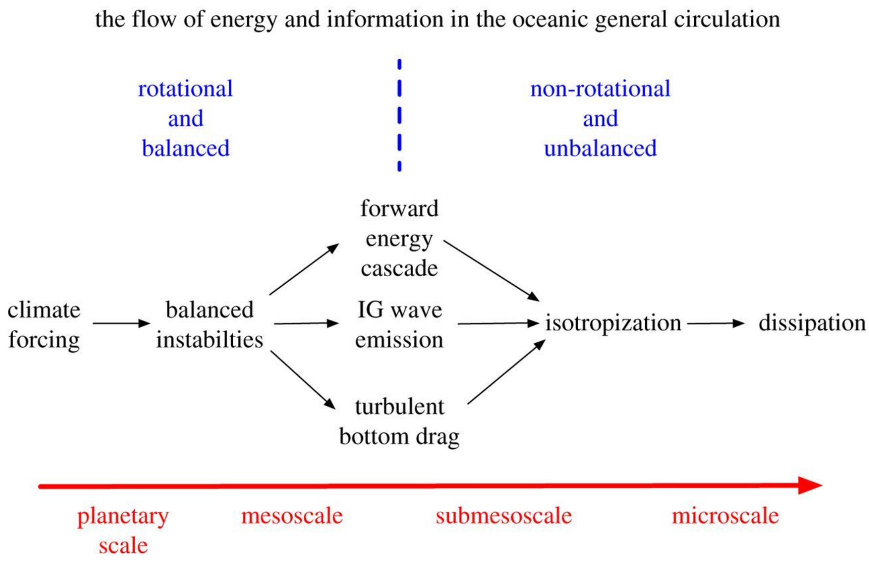

FIGURE 1.2: Dissipation scheme in the ocean from planetary scale to microscale. (McWilliams, 2016)

The different scales can be studied using the Rossby number:

$$\mathrm{Ro} = \frac{U}{fL}, \tag{1.1}$$

the ratio of the inertial force (momentum advection) to the Coriolis force, where U is the flow velocity scale, L is the length scale, and f the Coriolis parameter. For large-scale flows, the length scale being typically of $\mathcal{O}(1000\text{ km})$ and the flow velocity quite small, the Rossby number is very small. The Rossby number increases with decreasing scales, and pass through $\mathcal{O}(1)$ at the submesoscale regime. Flows with sufficiently small Rossby number are said to be in geostrophic balance, meaning that the pressure gradient is balanced by the Coriolis term, yielding:

$$\vec{u}_g = \frac{1}{f\rho}\vec{k} \times \nabla p, \tag{1.2}$$

where the subscripts g stands for geostrophic. A geostrophic flow moves along isobars with the lower (higher) pressure on its right (left) in the Northern (Southern) Hemisphere. In the ocean interior, away from the equator ($f \neq 0$), the flow is usually geostrophic. The geostrophic velocities can be derived from the sea surface height η, usually known from satellite altimetry data:

$$-fv_g = -g\frac{\partial \eta}{\partial x} \tag{1.3}$$

$$fu_g = -g\frac{\partial \eta}{\partial y} \tag{1.4}$$

Thus, it is possible to deduct the flow trajectory by looking at the sea-surface height, and vice-versa. Assuming a geostrophic component of the flow, the total flow velocity can therefore be decomposed into a geostrophic (g), and an ageostrophic (ag) component:

$$\vec{u} = \vec{u}_g + \vec{u}_{ag} \tag{1.5}$$

Mesoscale flows are mainly geostrophic, and ageostrophy appears for large Rossby numbers, starting from the submesoscales. In order to genuinely understand the submesoscale regime and its underlying mechanisms, we begin with thoroughly describe the large-scale and mesoscale regimes, and then transition to a description of the submesoscale dynamics.

1.1.1 Large-scale circulation

The ocean circulation can be described to a good approximation by the primitive equations, *i.e.* the Navier-Stokes equations, in addition to a nonlinear equation of state, hence coupling the fluid velocity to the active tracers. Assuming the fluid to be incompressible:

$$\nabla \cdot \vec{u} = 0, \tag{1.6}$$

the ocean flow, at all scales, then obeys to the momentum equation:

$$\frac{D\vec{u}}{Dt} + 2\vec{\Omega} \times \vec{u} = -\frac{1}{\rho}\nabla p - \vec{g} + \mathcal{F} \tag{1.7}$$

the mass conservation equation:

$$\frac{D\rho}{Dt} + \rho\nabla \cdot \vec{u} = 0 \tag{1.8}$$

the equation of state:

$$\rho = \rho(T, S, p) \tag{1.9}$$

and the thermodynamics equation:

$$\frac{DQ}{Dt} = c_p \frac{DT}{Dt} - \frac{1}{\rho}\frac{Dp}{Dt} \tag{1.10}$$

where $\vec{u}$ is the full velocity vector (u, v, w) in the zonal, meridional and vertical directions respectively, $\vec{\Omega}$ is the angular velocity vector, ρ is the density of sea water, p is the pressure, $\mathcal{F}$ is the friction term, g is the gravitational force acting on the fluid, Q is the heat and T the temperature. The time rate of change of a certain variable within a fluid parcel, as it flows along its pathline, is described by the material derivative:

$$\frac{D}{Dt} \equiv \frac{\partial}{\partial t} + \vec{u} \cdot \nabla \tag{1.11}$$

The second term of the momentum equation ($\vec{\Omega} \times \vec{u}$), in a rotating frame of reference, is the Coriolis force. It can be approximated by:

$$2\vec{\Omega} \times \vec{u} \approx f\vec{k} \times \vec{u} \tag{1.12}$$

where $f \equiv 2\vec{\Omega} \sin\phi$, is the Coriolis parameter and ϕ the latitude. f is greater at the poles and changes sign at the equator. The friction term $\mathcal{F}$ comprises the wind-stress and the viscosity. The viscosity includes the molecular viscosity, and the eddy viscosity, referring to the transfer of momentum to the fluid by turbulent eddy mixing. The eddy viscosity is mathematically described by a horizontal eddy viscosity term (A_H) and a vertical eddy viscosity term (A_V).

Using scale analysis, we can simplify the momentum equation for large-scale motions, considering these characteristic scales for mid-latitude ($\phi \sim 45°$) synoptic systems:

U	$\sim 0.1 - 1\ \mathrm{ms}^{-1}$	horizontal velocity scale
W	$\sim 10^{-5}\ \mathrm{ms}^{-1}$	vertical velocity scale
L	$\sim 10^{6}\ \mathrm{m}$	horizontal length scale
H	$\sim 10^{4}\ \mathrm{m}$	depth scale
$\delta P/\rho$	$\sim 10^{3}\ \mathrm{m^2s^{-2}}$	horizontal pressure fluctuation scale
$T \sim L/U$	$\sim 10^{5}\ \mathrm{s}$	time scale

The scale analysis for the horizontal component of the momentum equation is:

$$\underbrace{\frac{\partial u}{\partial t}}_{\frac{U}{T}\sim 10^{-6}} + \underbrace{u\frac{\partial u}{\partial x}}_{\frac{UU}{L}\sim 10^{-8}} + \underbrace{w\frac{\partial u}{\partial z}}_{\frac{WU}{H}\sim 10^{-12}} = \underbrace{-\frac{1}{\rho}\frac{\partial p}{\partial x}}_{\frac{\delta P}{\rho L}\sim 10^{-3}} + \underbrace{fv}_{fU\sim 10^{-6}} \tag{1.13}$$

and the scale analysis for the vertical component of the momentum equation is:

$$\underbrace{\frac{\partial w}{\partial t}}_{\frac{W}{T}\sim 10^{-6}} + \underbrace{u\frac{\partial w}{\partial x}}_{\frac{UW}{L}\sim 10^{-12}} + \underbrace{w\frac{\partial w}{\partial z}}_{\frac{WW}{H}\sim 10^{-12}} = \underbrace{-\frac{1}{\rho}\frac{\partial p}{\partial z}}_{\frac{\delta P}{\rho H}\sim 10} - \underbrace{g}_{g\sim 10} \tag{1.14}$$

The advection terms for the horizontal velocities can be neglected, leaving us with a balance between the time-derivative of the horizontal velocity, the pressure gradient, and the Coriolis term. In a steady state ($\partial/\partial t = 0$), they become the equations of for the geostrophic balance. In the vertical, the first term and the advective terms can be neglected, leaving us with a balance between the vertical pressure gradient and the gravitational force, called the hydrostatic balance.

To sum up, these few assumptions can be made for the large-scale motions:

1. *Thin-shell approximation*: The ocean depth $\mathcal{O}$(4 km) is much smaller than the Earth's radius $\mathcal{O}$(6000 km), and therefore can be neglected.

2. *Hydrostatic approximation*: In the vertical equation of motion, the friction and the vertical acceleration are negligible, yielding a balance between the pressure gradient and the gravity, or the hydrostatic balance:

$$\frac{\partial p}{\partial z} = -\rho g \tag{1.15}$$

3. *Boussinesq hypothesis*: Density variations are neglected except in their contribution to the buoyancy force, where it appears in multiple of g.

4. *Large Reynolds number approximation*: Viscous terms are very small and can be neglected.

Following these assumptions, the simplified momentum equations for large-scale oceanic motions become:

$$\begin{aligned}
\frac{Du}{Dt} - fv &= -\frac{1}{\rho}\frac{\partial p}{\partial x} + \mathcal{F}_x \\
\frac{Dv}{Dt} + fu &= -\frac{1}{\rho}\frac{\partial p}{\partial y} + \mathcal{F}_y \\
0 &= -\frac{1}{\rho}\frac{\partial p}{\partial z} - g
\end{aligned}$$

These equations thoroughly describe the dynamics of a fluid in a thin spherical shell on a rotating sphere, for a slow and large-scale motion (Olbers, Willebrand, and Eden, 2012).

1.1.2 Mesoscale dynamics

Mesoscale fluctuations are almost always present in the ocean. They occur over time scales of $\mathcal{O}$(1 month) and have a typical horizontal spatial scale of $\mathcal{O}$(10-100 km). The scale of the mesoscale eddies is of the order of the first baroclinic Rossby radius of deformation (R_1), the horizontal scale at which rotational effects become as important as buoyancy effects (Chelton et al., 1998). Mesoscale eddies emerge from baroclinic and barotropic instabilities, and strong horizontal sheared motions applied on large-scale flows (Olbers, Willebrand, and Eden, 2012). These eddies often take the form of well defined rings extending to depths of hundreds to a thousand meters.

Using again the scaling analysis, we can simplify the momentum equations for the mesoscale. The characteristic scales for the mesoscale at mid-latitude are listed below. The arrows indicate a change in comparison to the large-scale motion.

U	$\sim 1\ \mathrm{ms}^{-1}(\uparrow)$	horizontal velocity scale
W	$\sim 10^{-4}\ \mathrm{ms}^{-1}(\uparrow)$	vertical velocity scale
L	$\sim 10^{5}\ \mathrm{m}\ (\downarrow)$	horizontal length scale
H	$\sim 10^{4}\ \mathrm{m}$	depth scale
$\delta P/\rho$	$\sim 10^{2}\ \mathrm{m}^2\mathrm{s}^{-2}(\downarrow)$	horizontal pressure fluctuation scale
$T \sim L/U$	$\sim 10^{4}\ \mathrm{s}\ (\downarrow)$	time scale

The scale analysis for the horizontal component of the momentum equation is:

$$\underbrace{\frac{\partial u}{\partial t}}_{\frac{U}{T}\sim 10^{-4}} + \underbrace{u\frac{\partial u}{\partial x}}_{\frac{UU}{L}\sim 10^{-5}} + \underbrace{w\frac{\partial u}{\partial z}}_{\frac{WU}{H}\sim 10^{-8}} = \underbrace{-\frac{1}{\rho}\frac{\partial p}{\partial x}}_{\frac{\delta P}{\rho L}\sim 10^{-3}} + \underbrace{fv}_{fU\sim 10^{-4}} \tag{1.16}$$

Here again, neglecting terms of smaller amplitude, we get the geostrophic balance. In certain cases, the horizontal and vertical velocities become more important, and only then all the terms in the equation are of the same amplitude, therefore none of them can be neglected and we are in *quasigeostrophy* (QG).

The scale analysis for the vertical component of the momentum equation is:

$$\underbrace{\frac{\partial w}{\partial t}}_{\frac{W}{T}\sim 10^{-9}} + \underbrace{u\frac{\partial w}{\partial x}}_{\frac{UW}{L}\sim 10^{-9}} + \underbrace{w\frac{\partial w}{\partial z}}_{\frac{WW}{H}\sim 10^{-12}} = \underbrace{-\frac{1}{\rho}\frac{\partial p}{\partial z}}_{\frac{\delta P}{\rho H}\sim 10} - \underbrace{g}_{g\sim 10} \tag{1.17}$$

The vertical acceleration is much smaller than the vertical pressure gradient and the gravitational terms, which are of same magnitude, hence the hydrostatic balance holds for mesoscale processes. The vertical motion is much smaller than the horizontal motion, hence the mesoscale flow is quasi-two-dimensional.

Quasigeostrophic potential vorticity

Mesoscale dynamics can be understood by studying the governing equations for oceanic flow with the quasigeostrophic theory, especially in cases where the horizontal and vertical velocities become more important. Geostrophy refers to a balance between the Coriolis force and the pressure gradient forces, while quasigeostrophy assumes an almost balance between those forces, with inertia having an effect. It approximates the equations of motion for a highly stratified fluid in rotation, with small Rossby number. It allows the Coriolis parameter to vary ($f = f_0 + \beta y$). With these assumptions, Olbers, Willebrand, and Eden, 2012 derives an equation for the conservation of the quasigeostrophic potential vorticity q:

$$\frac{Dq}{Dt} = 0, \qquad q = \beta y + \nabla_h^2 \psi + \frac{\partial}{\partial z}\left(\frac{f_0}{N^2}\frac{\partial \psi}{\partial z}\right) \tag{1.18}$$

The equation for the potential vorticity states that the summation of the planetary vorticity (first term), the relative vorticity (middle term), and the stretching vorticity (last term) is constant following a quasigeostrophic flow. f_0 is the Coriolis parameter at latitude ϕ_0, $\beta = (df/dy)|_{\phi_0} = 2\Omega\cos(\phi_0)/R_E$ is the Rossby parameter, y is the meridional distance from ϕ_0, Ω is the angular rotation rate of the Earth, R_E is the Earth's radius, and the squared Brünt-Väisälä frequency

$$N^2 = -\frac{g}{\rho_0}\frac{\partial \rho}{\partial z} \tag{1.19}$$

is a measure of seawater stratification. The stream function ψ determines the entire flow at any instant:

$$u = -\frac{\partial \psi}{\partial y} \tag{1.20}$$

$$v = +\frac{\partial \psi}{\partial x} \tag{1.21}$$

$$w = -\frac{f_0}{N^2}\frac{D}{Dt}\frac{\partial \psi}{\partial z} - \frac{g\mathcal{G}_\rho}{N^2} \tag{1.22}$$

$$\rho = -\frac{f_0}{g}\frac{\partial \psi}{\partial z} \tag{1.23}$$

Rossby radii of deformation

Chelton et al., 1998 demonstrated the that baroclinic Rossby radii of deformation can be obtained by linearizing the quasigeostrophic potential vorticity equation (Eq.1.18) about a zero background mean flow. Assuming the absence of buoyancy forcing, wind stress, or frictional forces, and a separable vertical velocity

$$w(x, y, z, t) = \phi(z)W(x, y, t), \tag{1.24}$$

then solving a Sturm-Liouville eigenvalue problem for the vertical structure of the vertical velocity, $\phi(z)$. The ordinary differential equation to solve, with inverse eigenvalue c_m of normal modes m, is the following:

$$\frac{d^2\phi}{dz^2} + \frac{N^2(z)}{c^2}\phi = 0 \tag{1.25}$$

The boundary conditions are vertical velocity vanishing at the sea surface and ocean bottom

$$\phi(0) = \phi(H) = 0, \tag{1.26}$$

where H is the mean water depth. At latitudes outside of the Tropics (about or greater than 5°, the Rossby radii of deformation are

$$R_m = \frac{c_m}{|f|}, \quad m = 0, 1, 2, ... \tag{1.27}$$

The analytical solution can be found using the so-called Wentzel-Kramers-Brillouin (WKB) approximation. Using this method, the first baroclinic Rossby radius of deformation outside of the equatorial band is

$$R_1 \approx R_1^{WKB} = \frac{1}{|f|\pi} \int_{-H}^{0} N(z)dz \tag{1.28}$$

The WKB method is only valid for a weakly varying N^2, which is usually not the case within the upper layer. More acceptable results for the upper ocean are obtained using a numerical integration scheme for estimating the speed velocity c_m.

As an example, Chelton et al., 1998 found that the baroclinic Rossby radius of deformation in the Caribbean Sea is 60-80 km.

1.1.3 Submesoscale dynamics

Submesoscale processes have an horizontal length scale of $\mathcal{O}$(1-10 km) and occur on time scales of hours to days. They are characterized by enhanced vertical velocities, strong vorticity, and they mainly affect the upper-ocean dynamics (Thomas, Tandon, and Mahadevan, 2008). The characteristic scales of the submesoscale motions are listed in the following table, with arrows representing the changes in relation to the mesoscale:

U	~ 10 ms$^{-1}(\uparrow)$	horizontal velocity scale
W	~ 10 ms$^{-1}(\uparrow)$	vertical velocity scale
L	$\sim 10^4$ m $(\downarrow)$	horizontal length scale
H	$\sim 10^4$ m	depth scale
$\delta P/\rho$	$\sim 10^2$ m^{2}s^{-2}	horizontal pressure fluctuation scale
$T \sim L/U$	$\sim 10^3$ s $(\downarrow)$	time scale

The scale analysis for the horizontal component of the momentum equation is:

$$\underbrace{\frac{\partial u}{\partial t}}_{\frac{U}{T}\sim 10^{-2}} + \underbrace{u\frac{\partial u}{\partial x}}_{\frac{UU}{L}\sim 10^{-2}} + \underbrace{w\frac{\partial u}{\partial z}}_{\frac{WU}{H}\sim 10^{-2}} = \underbrace{-\frac{1}{\rho}\frac{\partial p}{\partial x}}_{\frac{\delta P}{\rho L}\sim 10^{-2}} + \underbrace{fv}_{fU\sim 10^{-3}} \tag{1.29}$$

The Coriolis force is one order of magnitude smaller than the other terms, hence can be neglected. The flow is ageostrophic.

The scale analysis for the vertical component of the momentum equation is:

$$\underbrace{\frac{\partial w}{\partial t}}_{\frac{W}{T}\sim 10^{-2}} + \underbrace{u\frac{\partial w}{\partial x}}_{\frac{UW}{L}\sim 10^{-2}} + \underbrace{w\frac{\partial w}{\partial z}}_{\frac{WW}{H}\sim 10^{-2}} = \underbrace{-\frac{1}{\rho}\frac{\partial p}{\partial z}}_{\frac{\delta P}{\rho H}\sim 2\times 10^{-2}} - \underbrace{g}_{g\sim 3\times 10^{-2}} \tag{1.30}$$

The vertical acceleration term is important, thus the hydrostatic approximation is no longer applicable. Submesoscale motions have to be considered as 3-dimensional.

General characteristics

Submesoscale processes develop from vigorous and unstable mesoscale eddies. They show significant departures from geostrophy, hence their large Rossby number ($|\mathrm{Ro}|>1$). In this context, the Rossby number, the ratio of inertial force to Coriolis force, can be computed using the relative vorticity scaled by the Coriolis parameter:

$$Ro = \frac{\zeta_z}{f}, \tag{1.31}$$

Submesoscale processes have Ro $\equiv \mathcal{O}(1)$, meaning that inertial motions overcome the planetary force, leading to ageostrophy.

Klein et al., 2007 studied the upper ocean turbulence and showed that with a 2$\times$2 km resolution numerical simulation of a nonlinear baroclinic unstable flow, the relative vorticity in the upper ocean layer exhibits large coherent structures, but with strong variability at the submesoscales (8-20 km), consisting of thin filaments and small vortices (see Fig.1.3). In the ocean interior, at 800 m, the relative vorticity field is dominated by larger vortices (>100 km) and thicker filaments, more a mesoscale aspect. The vertical profiles of kinetic energy of their submesoscale permitting simulations highlighted this difference by showing a clearly more energetic upper ocean, with most of the energy trapped within the first 1000 m and the maximum located at the surface. The vertical profile of the enstrophy, quantity interpreted as the mean Rossby number ($\sqrt{\langle\zeta_z^2\rangle}/f_0$), was relatively large near the surface (close to 0.3), and much smaller towards the interior (0.03).

The vorticity and w distributions are highly asymmetric with long tails and exhibit significant skewness in favor for cyclonic vorticity and downward motions (Fig.1.4). The positive skewness is explained by the fact that there are submesoscale instabilities that occur when $\zeta_z/f <$ -1 but do not occur for $\zeta_z/f > 1$. These asymmetries should essentially be absent before the submesoscale transition, and deeper after the transition (Capet et al., 2008c).

The breakage of the geostrophic balance led by submesoscale processes initiates a forward energy cascade: smaller eddies dissipate the energy absorbed from large, very energetic eddies. This cascade is visible from the energy spectrum. The concepts of turbulence and energy cascade were first explained qualitatively by Richardson (1922), and quantitatively by Kolmogorov (1941). The theory of turbulence will

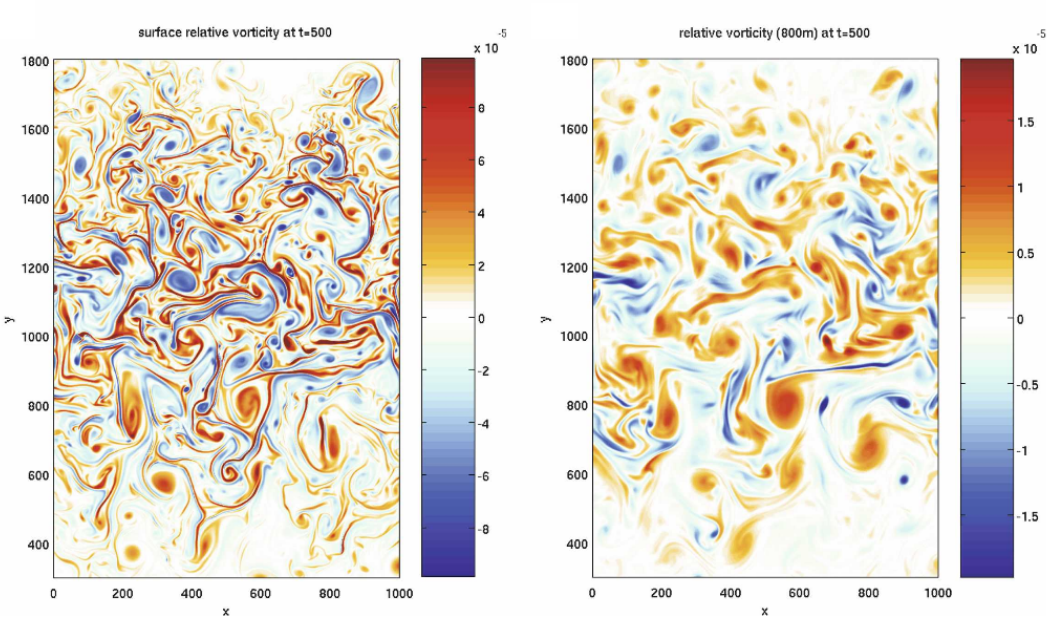

FIGURE 1.3: Instantaneous relative vorticity at the surface (left) and at 800 m (right). Klein et al., 2007.

not be explained here as it is beyond the scope of this thesis. Charney, 1971 argued that quasigeostrophic turbulence leads to a kinetic energy and tracer variance horizontal and vertical wavenumber spectra converging towards k^{-3}, and this was confirmed in the oceanic context from numerical simulations of a two-dimensional mesoscale flow field (Capet et al., 2008a, Klein et al., 2007).

Capet et al., 2008a studied the mesoscale to submesoscale transition in the Californian Current System, with five cases differing in their horizontal gridpoint spacing: 12, 6, 3, 1.5, and 0.75 km. Their results showed that with a three-dimensional finer resolution simulations, when resolving submesoscale processes, this led to a flattening of the kinetic energy spectrum slope to -2 (Fig.1.5) which indicated a significant degree of kinetic energization in the submesoscale regime in the upper ocean layer (Capet et al., 2008a). The subsurface kinetic spectrum slopes remain steeper than -3, expressing that it undergoes a less dramatic change.

of the mixed-layer depth (MLD), and the horizontal scale is of the order of the mixed-layer Rossby radius of deformation:

Mathematical framework

After Mahadevan and Tandon, 2006 and Thomas, Tandon, and Mahadevan, 2008. Submesoscale flows are characterized by a Rossby number and a Richardson number of $\mathcal{O}(1)$. The latter is expressed as the following:

$$Ri = \frac{N^2}{|\partial \mathbf{u}_h|} \tag{1.32}$$

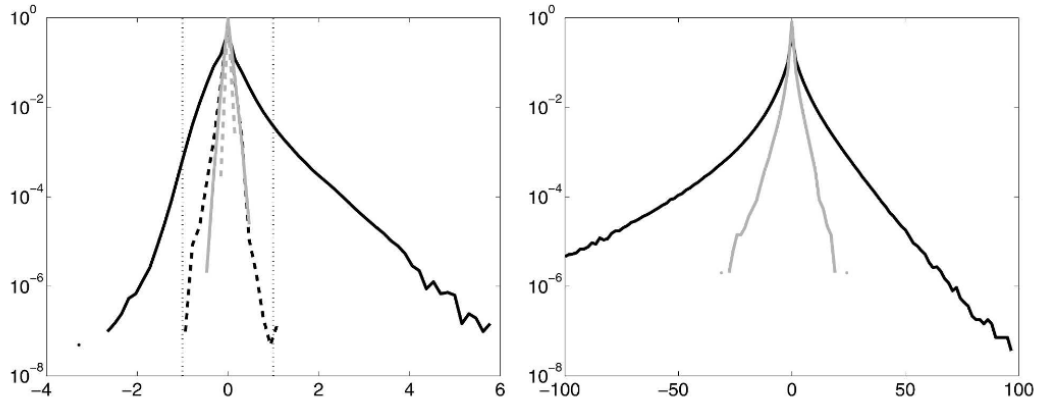

FIGURE 1.4: From Capet et al., 2008a. PDFs for (left) ζ_z/f_0 at 10 (solid line) and 70 m depth (dashed line) and (right) w (day^{-1}) at 20 m depth at 0.75 (black lines) and 6 km resolution (gray lines).

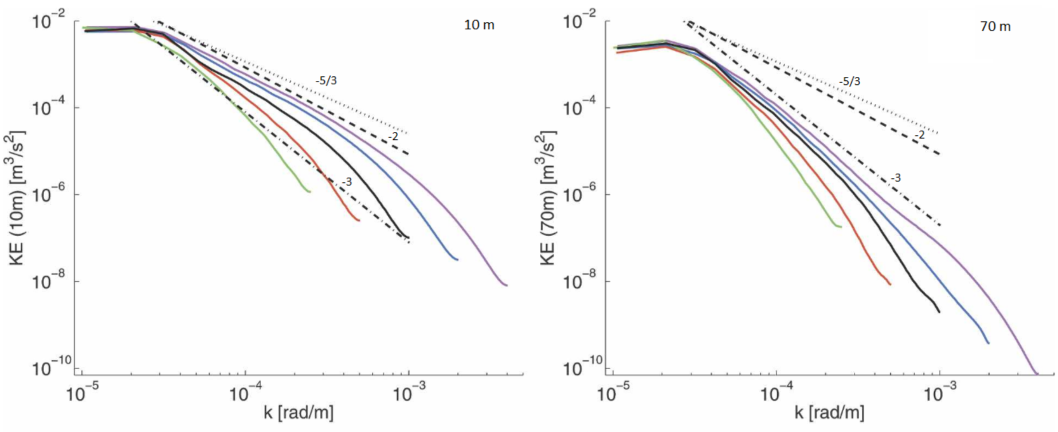

FIGURE 1.5: Wavenumber spectra for horizontal velocity (u, v) at (left) 10 and (right) 70 m depth. Straight lines indicate the -5/3, -3 and -2 spectrum slopes, and the five curves correspond to different cases with different resolutions. Capet et al., 2008a.

The Richardson number is essentially a ratio between potential and kinetic energies, with the numerator being the potential-energy barrier that mixing must overcome, and the denominator being the kinetic energy that the shear flow can supply when smoothed away (Cushman-Roisin and Beckers, 2011 §14.2). The denominator is the square of the vertical shear:

$$\mathrm{Sh} = \left(\frac{\partial u}{\partial z}^2 + \frac{\partial v}{\partial z}^2 \right) \tag{1.33}$$

Submesoscale flows are, to a large extent, balanced. This means that its dynamics can be described by a single scalar field. However, the geostrophic balance is a too simple model, and the values for Ro and Ri, both being of $\mathcal{O}(1)$ unable us to use the quasigeostrophic (QG) model. The *semigeostrophic* (SG) model has been found to describe more accurately the dynamics of submesoscales and giving an insight into the dynamics of typical submesoscale features such as intense fronts and vertical circulations. In the SG theory, the flow is decomposed into geostrophic and ageostrophic components $\vec{u} = \vec{u_g} + \vec{u_{ag}}$, where the geostrophic velocities can be found using the geostrophic balance. The SG equations are:

$$\frac{D\vec{u}_g}{Dt} = -f(\hat{k} \times \vec{u}_{ag}) \tag{1.34}$$

$$0 = -\frac{1}{\rho_0}\frac{\partial p}{\partial z} + b \tag{1.35}$$

$$\frac{Db}{Dt} = 0 \tag{1.36}$$

$$\nabla \cdot \vec{u}_{ag} = 0, \tag{1.37}$$

with b the buoyancy.

Submesoscale processes can also be understood in terms of the Ertel's potential vorticity (PV):

$$q = (f + \zeta_z)N^2 + \vec{\omega}_h \cdot \nabla_h b, \tag{1.38}$$

where

$$\vec{\omega}_h = \left(\frac{\partial w}{\partial y} - \frac{\partial v}{\partial z}\right)\hat{\imath} - \left(\frac{\partial w}{\partial x} - \frac{\partial u}{\partial z}\right)\hat{\jmath} \tag{1.39}$$

and

$$\vec{\zeta}_z = \left(\frac{\partial v}{\partial x} - \frac{\partial u}{\partial y}\right)\hat{k} \tag{1.40}$$

are respectively the horizontal and vertical components of the vorticity of the flow $\vec{\omega}$, and $\nabla_h b$ is the horizontal buoyancy gradient. At large scales, q is dominated by the planetary vorticity fN^2 and at mesoscales, the vertical vorticity ζN^2 becomes important. Buoyancy gradients are important in the upper ocean, where density gradients arising from frontal filaments or outcropping isopycnals are non-negligible. In these cases, its contribution to the PV can be as large as the planetary PV, therefore considerably reducing the total PV.

Mechanisms generating submesoscale dynamics

Mahadevan and Tandon, 2006 analyzed different mechanisms for the generation of submesoscale vertical motion at ocean fronts. In an idealized experiment using a 500 m resolution grid, they observed the formation of mesoscale meandering density fronts as the flow evolved and became baroclinically unstable. Submesoscale structures appeared with an intensification in vertical velocities within the mixed-layer depth with intense downwelling (100 m/day) motions concentrated in narrow bands (2 km).

Several mechanisms have been proposed to explain the formation of submesoscale structures and their impact on the flow. High resolution modeling and analytical studies showed that both forced and unforced instabilities drive submesoscale motions. Some authors used idealized experiments (Klein et al., 2007, Brannigan et al., 2017, Mahadevan and Tandon, 2006), and recent publications showed real cases (Trotta et al., 2017) and even observations (Capet et al., 2008a).

1. *Frontogenesis*. In the ocean, fronts are boundaries between two different water masses that have different densities, very often associated with a large temperature gradient (Fig.1.6).

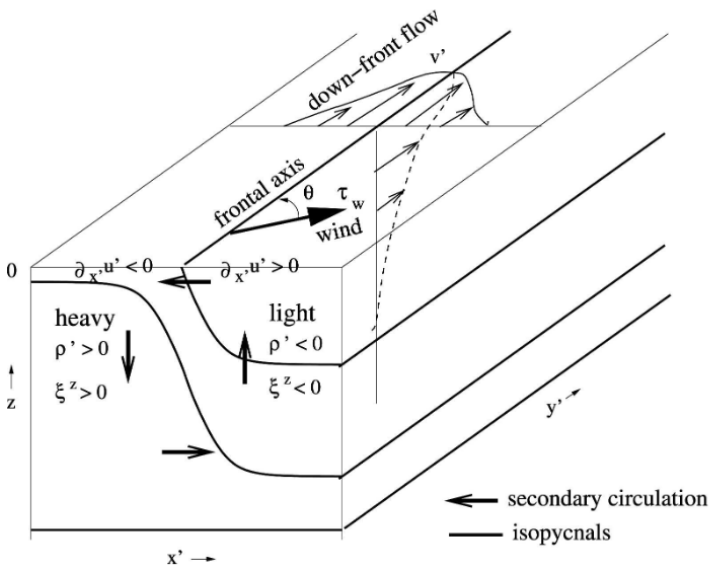

FIGURE 1.6: Schematic of an intensifying straight surface front for f>0. Capet et al., 2008c.

The generation of fronts, called frontogenesis, is stimulated by an intensification of horizontal density or temperature gradients due to the presence of a large-scale and mesoscale lateral strain (Hoskins and Bretherton, 1972). The lateral strain rate is a measure of the deformation with respect to time:

$$\mathrm{SR} = \left((u_x - v_y)^2 + (v_x + u_y)^2\right)^{1/2} \tag{1.41}$$

This horizontal shearing motion disrupts the geostrophic balance for the alongfront flow, and generates an ageostrophic secondary circulation, in the cross-front plane (Capet et al., 2008b). The secondary circulation tilts the isopycnals towards the horizontal (*i.e.* restratification) in order to restore the balance. At these sites, the strong secondary ageostrophic overturning circulation generates intense vertical velocities, and the Rossby number and the Richardson number become of $\mathcal{O}(1)$ (Thomas, Tandon, and Mahadevan, 2008). Restratification is a process where warmer and lighter waters lay over colder and denser waters, which happens trivially when the fluid is heated from above, but can also happen dynamically. The stratification of a water column can be studied using the Brunt-Väisälä frequency (N^2). Restratification driven by submesoscale baroclinic instabilities plays an important role in the heat and salt budget of the ML.

Thomas, Tandon, and Mahadevan, 2008 generated a submesoscale flow due to frontogenesis from an idealized simulation experiment. They initialized a numerical ocean model with an across-front density variation of 0.27 kg m^{-3}, a readily spontaneous frontogenesis, across 20 km over a deep mixed-layer of 250 m. As a result there was a localized intensification of buoyancy gradient, large Ro, small Ri, strong lateral strain rate, and enhancement of the vertical velocity.

Mahadevan and Tandon, 2006 studied the generation of submesoscale motions due to strain driven frontogenesis, using an idealized model. They examined the relationship between the horizontal strain rate, the relative vorticity, and submesoscale vertical velocities (see Fig. 1.7). They observed a preponderance of cyclonic vorticity (Ro>0), which can be explained by the SG dynamics, where the rate of growth of cyclonic/anticyclonic motions is asymmetric. Regions of high strain is associated with large relative vorticity, and regions of high cyclonic vorticity are associated with intense downwelling (negative vertical velocities). High strain rate and large Rossby number are found at regions where submesoscale downwelling occurs.

2. *Forced motions*. Destabilizing atmospheric forcing such as buoyancy fluxes (heat and salt fluxes) or down-front wind stress can lead to creation of submesoscale eddies. Both tend to reduce the stratification (hence the Richardson number), as well as the potential vorticity (PV) of the upper ocean (Thomas, Tandon, and Mahadevan, 2008). As an example for the buoyancy loss forcing, Legg and McWilliams, 2001 observed that, for an idealized case, cooling of barotropic eddies triggered submesoscale eddies that led to a much faster increase in barotropic eddy kinetic energy than in the case where there was no cooling, suggesting that cooling could be a pathway for the conversion of available potential energy to barotropic eddy kinetic energy, leading to restratification of the upper-ocean.

3. *Mixed layer instabilities*. Submesoscale processes within the mixed-layer tend to increase stratification. The mixed-layer (ML) is the upper-ocean layer where ocean properties and momentum are homogenized by active turbulent processes that cause mixing. The water density, highly correlated to temperature by the state function, has also a reduced vertical gradient within this layer, and increases dramatically at the pycnocline (the depth at which the density gradient is maximum), usually located below the mixed-layer depth (MLD). The work of Boccaletti, Ferrari, and Fox-Kemper (2007) showed that within the ML, baroclinic instabilities develop as a consequence of density fronts out of the geostrophic balance, resulting in the formation of submesoscale eddies of size 1-10 km that act to continuously restratify the surface mixed-layer. Baroclinic instabilities draw its energy from the potential energy of the unperturbed flow

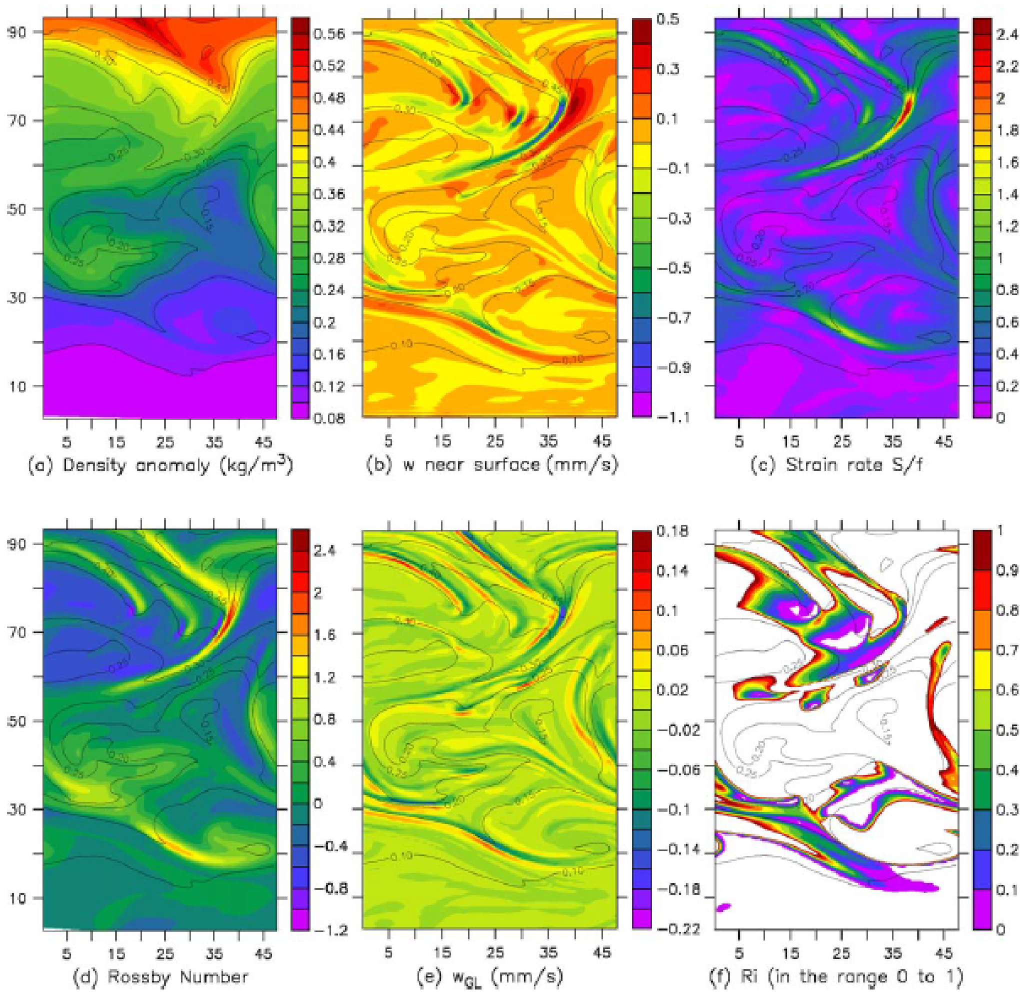

FIGURE 1.7: Near surface field (15 m) from day 44 of the simulation. (a) surface density anomaly, (b) vertical velocity, (c) normalized strain rate S/f, (d) local Rossby number calculated as $Ro = \zeta/f$, (e) an estimate of the vertical velocity due to frictional effects at fronts, and (f) Richardson number in the range 0-1. Mahadevan and Tandon, 2006.

and the disturbances grow at a scale rate near the local first baroclinic Rossby radius of deformation (Stone, 1966).

4. *Ageostrophic anticyclonic instability and loss of balance*. The three main routes for energy dissipation from a balanced flow through the loss of balance are: (i) change in sign of the absolute vorticity A, (ii) change in sign of the vertical buoyancy gradient N, which gives rise to convective motions, or (iii) change in sign of the difference between the absolute vorticity and the strain rate $A - S$, where unbalanced ageostrophic instabilities develop (McWilliams, Molemaker, and Yavneh, 2001). Molemaker, McWilliams, and Yavneh, 2005 show that in regions where the local Rossby number is large, ageostrophic anticyclonic baroclinic instability can arise spontaneously at submesoscales from

a loss of balance yielding a forward energy cascade. Mahadevan and Tandon, 2006 tested whether ageostrophic baroclinic instabilities play a role in setting up submesoscale structures in regions where loss of balance occurs. They found that the region where $A - S$ changes sign coincides with the most intense downwelling site in the domain. They concluded that this suggest that the conditions are appropriate for the loss of balance and the development of ageostrophic anticyclonic instability.

5. *Nonlinear Ekman effect*. Down-front winds can generate intense downwelling due to cross-front Ekman transport at the surface Thomas and Lee, 2005. This downward motion induces localized mixing and an additional secondary ageostrophic circulation, reducing stratification (and Ri) in the surface boundary layer, thus providing favorable conditions for submesoscale processes.

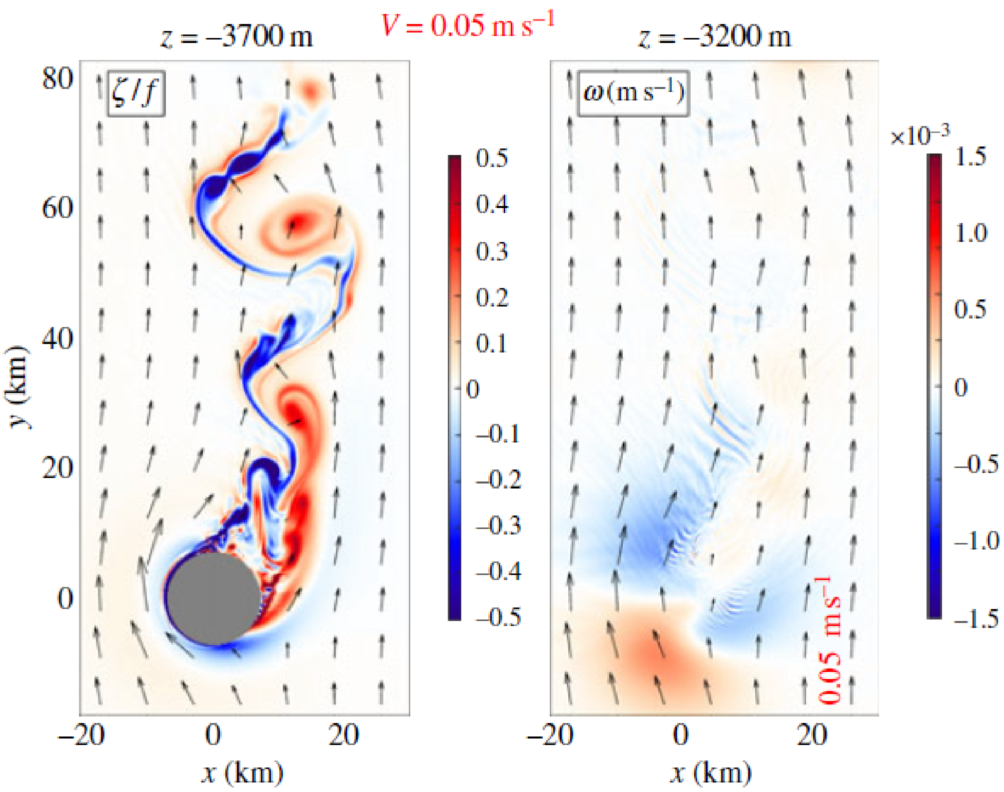

FIGURE 1.8: Topographic wakes in an idealized experiment generated by the interaction between an incoming flow and a seamount. McWilliams, 2016.

6. *Topographic wakes*. Submesoscale motions can arise from the interaction between the oceanic flow and the topography (Fig.1.8). The snapshot shows the result of an idealized configuration of uniform stratification by McWilliams, 2016. The flow, with velocity of 0.05 ms^{-1}, is induced with vorticity at the contact with the boundary, and subsequent rollups due to barotropic centrifugal-instabilities lead to a significant input of vorticity into the basin through the

formation of submesoscale coherent vortices. The vortical flow shows an impact on the vertical velocity up to 500 m above. In the real ocean, both the incoming flow and the boundary shape are non-uniform in z, making the so-called wakes and their evolution fully tree-dimensional.

1.2 Mesoscale variability in the Caribbean Sea

The Caribbean is a semi-enclosed sea delimited by Central America, and the northern part of South America (see Fig.1.9). It spans over 3500 km of longitude and 2500 km of latitude, and is separated from the Atlantic Ocean by the closely spaced chain of Antilles Islands. The Caribbean Sea is important in terms of mesoscale dynamics, as its location within Central America allows the propagation of mesoscale eddies through its whole basin, forming a connection between the Southern and Northern Atlantic oceans, hence interacting with the Atlantic Meridional Overturning Circulation (AMOC).

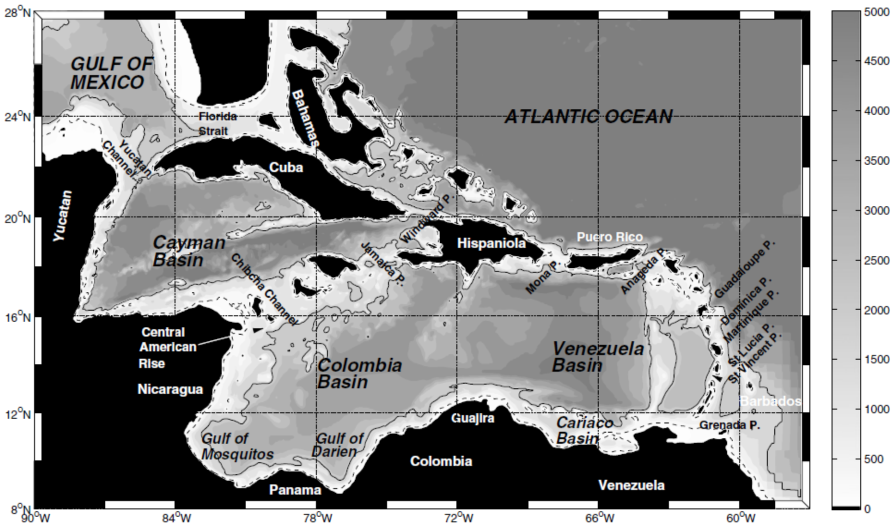

FIGURE 1.9: Map and bathymetry of the Caribbean Sea. Jouanno et al., 2008.

The Caribbean Sea water inflow comes from the Subtropical Gyre (SG), the North Equatorial Current (NEC) and the North Brazil Current (NBC). At the eastern side of the Sea, those waters merge and form the Caribbean Current, composed of two jets flowing westwards along the southern and the northern boundaries of the Venezuela Basin: the southern Caribbean Current (sCC) and the northern Caribbean Current (nCC), respectively. As the sCC reaches the Colombia Basin, it divides into two branches. The southward branch feeds the cyclonic Panama Colombia Gyre, itself providing for the eastward Caribbean Coastal Undercurrent (CCU), located around 200 m depth (Andrade, Barton, and Mooers, 2003). The northward branch of the sCC, larger and more energetic, merges with the nCC and together they flow to the Gulf of Mexico mostly channeling through a trough southwest of Jamaica, and then flow out through the Yucatan Channel (see Fig. 1.10). The main propagation speed of the Caribbean Current is about 0.3 ms^{-1}, with the highest surface velocities of 0.6-0.7 ms^{-1} found at Maracaibo and along Panama due to a northward deflection caused by the geography of the coastline (Fratantoni, 2001).

Jouanno et al., 2008 investigated the mesoscale variability in the Caribbean Sea using a $1/15°$ resolution general circulation model and found that the mean current path near the Lesser Antilles at 30 m depth is dominated by a narrow and strong flow through the Grenada Passage and a secondary flow through St-Vincent and St-Lucia Passages. Both flows come from the return flow of the AMOC. At 150 m, the inflow through the Grenada Passage is absent and the water input comes from the southern branch of the Subtropical Gyre. The signature of both contributions is well represented on mean Sea Surface Height (SSH) maps. The interaction and merging of the two water contributions conjugated to the instability of the jet flowing through the Grenada Passage is mainly responsible for the production and growth of strong and deep baroclinic eddies within the Caribbean Sea.

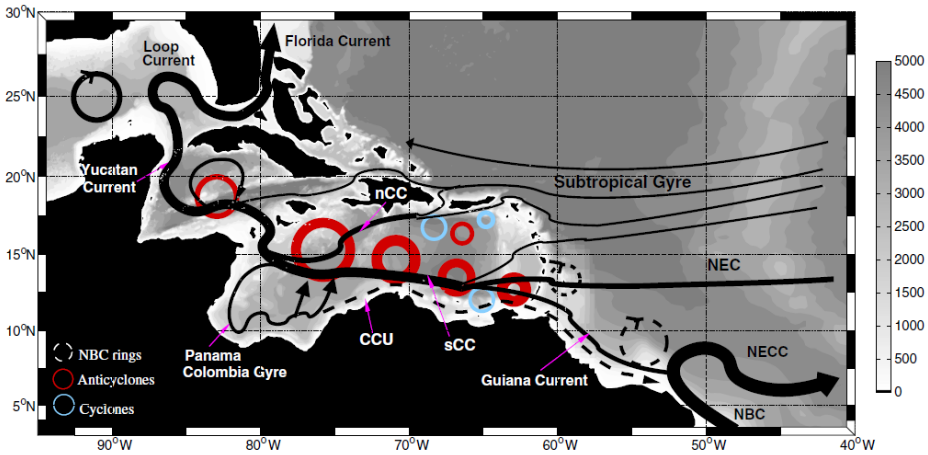

FIGURE 1.10: Main current paths of the Caribbean Sea. Jouanno et al., 2008.

The Caribbean Sea is home to a strong and energetic mesoscale activity. While most of the eddies are anticyclonic, we also find smaller and weaker cyclonic eddies, mainly located near the South American coast or at the northern part of the Venezuela Basin. Large and energetic anticyclones eddies form and propagate with the Caribbean Current westward with speeds of 0.06-0.15 ms^{-1} and maximum swirl speeds of 0.3-0.6 ms^{-1} (Jouanno et al., 2008). They have a diameter of 200-500 km and a coherent vertical structure down to 1000 m depth. Richardson (2005) found that about 8-12 eddies per year were formed within the Caribbean Sea, with a maximum from September to November and a minimum from February to May, and for most eddies, the journey lasts about 10 months from the the Lesser Antilles to the Yucatan Channel.

The transport into the Caribbean Sea was estimated to be about 28 Sv, coming from three sources: the Windward Islands passages south of Martinique (∼10 Sv),

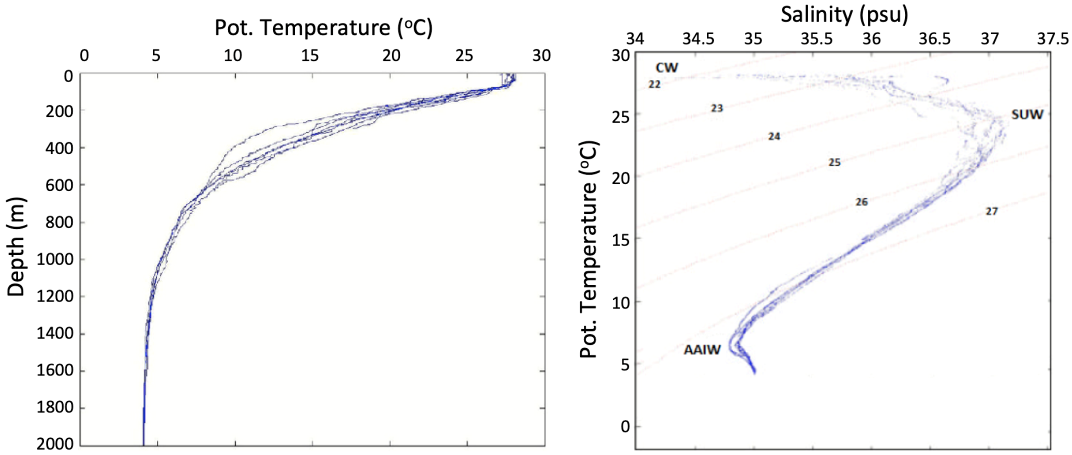

FIGURE 1.11: Temperature vertical profile (left) and T-S diagram (right) in the Caribbean Sea in summer. Observational data taken during the SO164 expedition. Nürnberg et al., 2002.

the Leeward Islands passages between Martinique and the Virgin Islands (~8 Sv), and the Greater Antilles passages between Puerto Rico and Cuba (~10 Sv) (Johns et al., 2002). The stratification of the water column in the Caribbean Sea is greatly influenced by the sill depth of the Antilles Islands arc, as it obstructs the inflow from the Atlantic ocean. Consequently, the upper 1200 m is highly stratified, between 1200 and 2000m it is weakly stratified, and below it is nearly homogeneous (Gordon, 1967).

The origin of the water masses can be obtained by studying the Temperature-Salinity (T-S) diagram, and their vertical profiles (Fig.1.11). Observations were taken from CTD stations during the expedition SO164 in the Caribbean Sea between May 22nd and June 28th, 2002. Water from both North and South Atlantic can be found. The Caribbean Surface Water (CW) occupies the upper 60 m of the water column and is composed of a mixture between the North Atlantic surface waters, the Amazon River water, and the local freshwater runoff from South America. The surface waters are therefore relatively fresh (<35.5 psu), and have a temperature of about 28°C. At about 150 m depth we find at the salinity maximum the Subtropical Under Water (SUW), a water mass formed in the central tropical Atlantic where evaporation is greater than precipitation, with salinity of >37 psu and temperature of 22-23°, also confirmed by Hernández-Guerra and Joyce (2000). The salinity minimum of 34.8 psu found around 800 m is the signature of the Antarctic Intermediate Water (AAIW).

The first baroclinic Rossby radius of deformation, the scale at which mesoscale dynamics such as mesoscale eddies develop, ranges between 60-80 km for the Caribbean Sea (Jouanno et al., 2008).

For a detailed description of the Caribbean Sea ocean currents and properties, see Gyory, Mariano, and Ryan (*The Caribbean Current. Ocean Surface Currents.*).

1.3 Objectives

In the present study, a submesoscale-permitting simulation is performed by one-way nesting in the Caribbean Sea in order to understand the implication of the change in horizontal resolution on the mesoscale flow. Increasing the horizontal resolution can affect the solution in space and time by permitting the emergence of features that are not resolved with coarser resolution models. Starting at $1/16°$resolution, the ocean dynamics is simulated for a limited time-period at $1/32°$ and $1/96°$ resolution via downscaling. This thesis aims to answer the following questions:

1. What horizontal resolution is needed for submesoscale motions to develop?
2. How long does it take for the solutions to decorrelate in time?
3. Which mechanisms generate the submesoscale motions?

It is important to acknowledge that this is not meant to be an extensive study of the submesoscale processes occurring in the Caribbean Sea, since the results come from only a limited running time-period of two weeks. This is a first approach to understand the possible implications of the submesoscale dynamics in the Caribbean Sea.

Chapter 2

Model and data

2.1 Numerical models

The simulations are performed using SURF (see Trotta et al., 2016), a NEMO-based numerical modelling platform that allows a grid refinement of the ocean dynamics, via downscaling. The data GOFS16 dataset is used as initial and boundary conditions to perform downscaling and to study the submesoscale dynamics in the Caribbean Sea. This section focuses on the models NEMO and the platform SURF. The implementation of SURF into the Caribbean Sea and the datasets used for the model validation are described further.

2.1.1 NEMO

NEMO is a free-surface, finite differences 3-D ocean model that solves the primitive equations, *i.e.* the Navier-Stokes equations combined with a nonlinear equation of state which couples the temperature and the salinity to the velocity of the fluid. In the solving of the primitive equations, the following assumptions are made:

1. *Spherical earth approximation*: geopotential surfaces are assumed to be spherical, so that gravity is parallel to the earth's radius.

2. *Thin-shell approximation* : the depth of the ocean is neglected compared to the radius of the earth.

3. *Turbulent closure hypothesis*: turbulent fluxes (effect of small scale processes on the large-scale) are expressed as a function of the mean flow.

4. *Boussinesq hypothesis*: density variations are ignored except where they appear in multiple of g, the gravitational acceleration.

5. *Hydrostatic hypothesis*: the vertical pressure gradient balances the buoyancy force.

6. *Incompressibility hypothesis*: the three dimensional divergence of the flow velocity is zero.

The complete system of equations to solve is:

$$\frac{\partial \vec{u}_h}{\partial t} = -\vec{\omega} \times \vec{u} - \frac{1}{2}\nabla(\vec{u}^2) - f\hat{k} \times \vec{u}_h - \frac{1}{\rho_0}\nabla_h p + \vec{D}^{\vec{u}} \tag{2.1}$$

$$\frac{\partial p}{\partial z} = -\rho g \tag{2.2}$$

$$\nabla \cdot \vec{u} = 0 \tag{2.3}$$

$$\frac{\partial \theta}{\partial t} = -\nabla \cdot (\theta \vec{u}) + D^T \tag{2.4}$$

$$\frac{\partial S}{\partial t} = -\nabla \cdot (S \vec{u}) + D^S \tag{2.5}$$

$$\rho = \rho(\theta, S, p) \tag{2.6}$$

where $\vec{u} = (u, v, w)$ and the subscript h indicate the horizontal field, $\vec{\omega} = \nabla \times \vec{u}$ is the vorticity, θ is the potential temperature, S the salinity, p the pressure, g the gravitational acceleration, f the Coriolis parameter, and $\vec{D}^{\vec{u}}$, D^T and D^S the parameterizations of small scale physics for $\vec{u}$, T and S respectively, including surface forcing terms, eddy viscosity coefficient and eddy diffusivity coefficient.

The model variables are computed on a horizontally and vertically staggered Arakawa-C grid (see Fig.2.1). The free surface, density and active tracers are located at the centre of the cell (T-grid), the horizontal u and v velocities are located respectively on the U- and the V-grid (left panel) and the vertical velocity w is located on the W-grid, at the bottom and top interfaces of the cell (right panel).

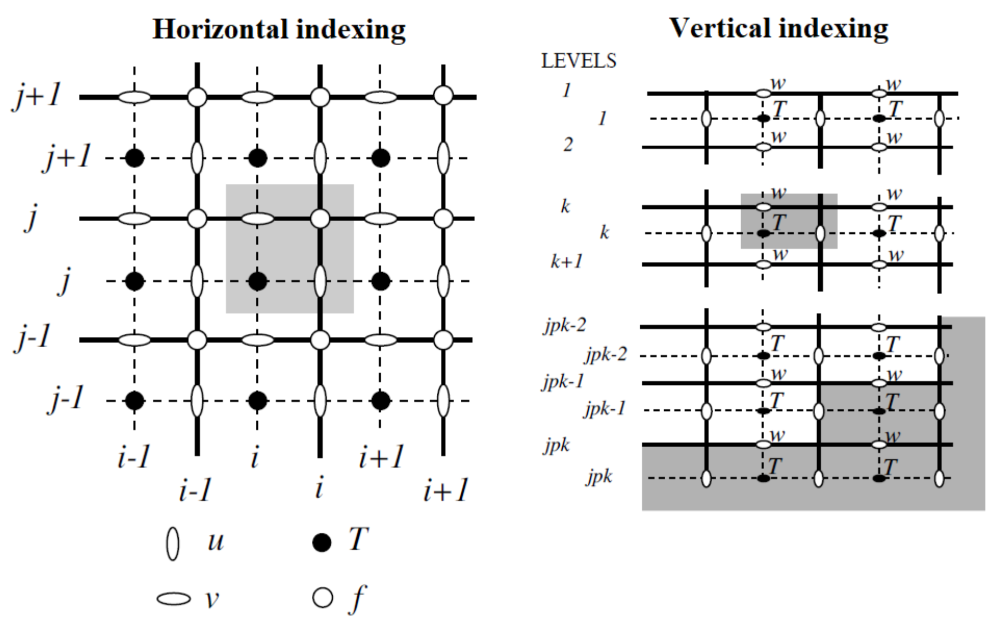

FIGURE 2.1: Structure and indexing of the Arakawa C-grid used by NEMO on the (left) horizontal and (right) vertical. Madec and NEMO team, 2008.

2.1.2 SURF

The Structured and Unstructured grid Relocatable ocean platform for Forecasting (hereafter SURF) is a numerical downscaling platform that does one-way nesting of the primitive-equation NEMO model (Trotta et al., 2016). It is working on a virtual machine environment. To enable the nesting in restricted area the modeling platform requires a high resolution bathymetry and a detailed coastal geometry, initial and boundary conditions from a large-scale model field (U, V, T, S and η), surface atmospheric forcing interpolated on the nested area, and specific model parameter settings. The parent model usually has a coarser horizontal and sometimes vertical resolution, and the numerical discretization and physical parameterizations can also be different. The parent provides initial and lateral boundary conditions for the SURF child components. The finer grid region is entirely embedded within the domain of the coarse grid region.

It first interpolates the parent model onto the new child grid, using bilinear interpolation on the horizontal, and linear interpolation on the vertical, and then extrapolates the new gridded data over land. This later serves as boundary and initial conditions for the numerical integration of the primitive equations.

The parameterization of the lateral subgrid-scale mixing of the active tracers and momentum are done using a horizontal biharmonic operator. The horizontal eddy diffusivity and viscosity coefficients are parameterized as a function of the parent coarser resolution model:

$$a_c = a_p \left(\frac{\Delta x_c}{\Delta x_p} \right)^4 \tag{2.7}$$

where the subscripts c and p stand for "child" and "parent". The vertical eddy viscosity and diffusivity coefficients are computed following the Richardson-number dependent scheme of Pacanowski and Philander (1981).

The density is computed after the nonlinear equation of state of Jackett and Mcdougall (1995):

$$\rho = \rho(\theta, S, p) \frac{\rho(\theta, S, 0)}{1 - p/K(\theta, S, p)}, \tag{2.8}$$

where $\rho(\theta, S, 0)$ is a 15-term polynomial and $K(\theta, S, p)$ is a 26-term polynomial. The depth-level formula is the same as used in the NEMO model:

$$z_0(k) = h_{sur} - h_0 k - h_1 \log\left[\cosh\left(k - h_{th}\right)/h_{cr}\right], \tag{2.9}$$

where h_{sur}, h_0 and h_1 have been determined through an optimization procedure (Madec and NEMO team, 2008 §4.3.2), h_{th} is the model level at which maximum stretching occurs, h_{cr} is the stretching factor ($\approx 3 - 10$), and k is the vertical index. Rather than entering the parameters h_{sur}, h_0 and h_1, it is possible to recalculate them. This approach consists in setting dz, the minimum thickness for the top layer, and h_{max}, the total depth of the ocean. Such an expression for the depth allows a nearly uniform vertical depth level discretization at the top and the bottom of the ocean,

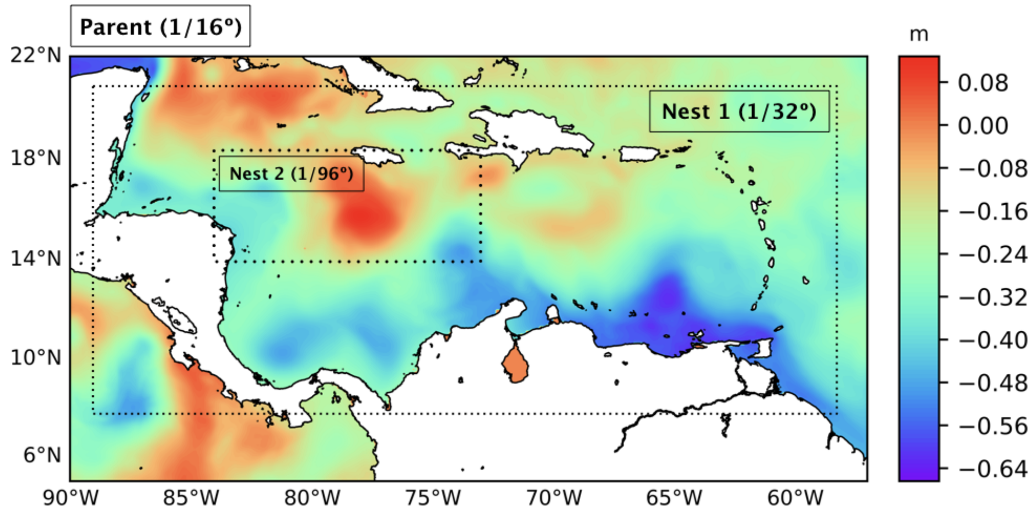

FIGURE 2.2: Nested regions shown on an instantaneous map of sea-surface height (m) of the parent model.

with a smooth transition in between, concentrating the vertical resolution near the ocean surface. The model uses partial cell discretization, so the bottom boundary layer thickness varies to better fit the bathymetry.

The time step is chosen so that the CFL condition is respected:

$$C = a\frac{\Delta t}{\Delta x} \leq 1 \longrightarrow \Delta t \leq \Delta x / a \tag{2.10}$$

with a, the numerical horizontal viscosity.

The lateral open boundary conditions are performed using the Flather radiation scheme for the barotropic velocities (Oddo and Pinardi, 2008), and the flow relaxation scheme for the baroclinic velocities (Madec and NEMO team, 2008 §8.4.2).

2.2 Implementation in the Caribbean Sea

The SURF platform was implemented in the Caribbean Sea, a region of highly variable bathymetry and energetic mesoscale activity. An experiment with two nestings has been performed within the selected time period of February 8th to 23rd, 2017, a choice motivated by the strong anticyclonic activity in the northern part of the basin, as seen on satellite data. The nested regions are presented in Fig.2.2.

2.2.1 Initial and boundary conditions

The dataset used for the parent model is the Global Ocean Forecasting System with $1/16^{\circ}$ resolution (GOFS16). It is based on NEMO v3.4 circulation ocean modeling system and assimilated salinity and temperature profiles, sea surface temperature, along track sea surface height, and sea-ice concentration on a daily basis. It has an horizontal spacing of 6.9 km at the equator and increasing poleward to $\sim$ 2 km. It has

98 uneven vertical levels with partial step. The bathymetry used is a combination of ETOPO2 for the deep ocean, GEBCO for the continental shelves, and BEDMAP2 for the Antarctica. The forecast system is forced with a 3-hourly momentum, radiation, precipitation fluxes from the operational Global Forecast System (GFS) fields. The outputs are a 1-day simulation of three-dimensional temperature, salinity, velocity fields, sea-surface height, and, sea ice thickness, concentration and driftand. It also produces a 6 days long forecast initialized by the former daily analysis. The data are available from 2017 to date. See Iovino et al., 2016 for more.

2.2.2 Atmospheric forcing

The atmospheric field is the Global Forecast System (GFS), a weather forecast model produced by the National Centers for Environmental Prediction (NCEP). The forecast system is forced with a 3-hourly momentum, radiation, precipitation fluxes fields. The surface-heat balance results from the atmospheric fluxes computed using the CORE bulk formulation, and there is no SSS restoring.

2.2.3 Bathymetry

The General Bathymetric Chart of the Oceans (GEBCO) is used for the bathymetry, a continuous terrain model for oceans and land at 30 arc-second interval ($\sim$ 830 m). The bathymetry in the Caribbean Sea domain is shown in Fig.1.9.

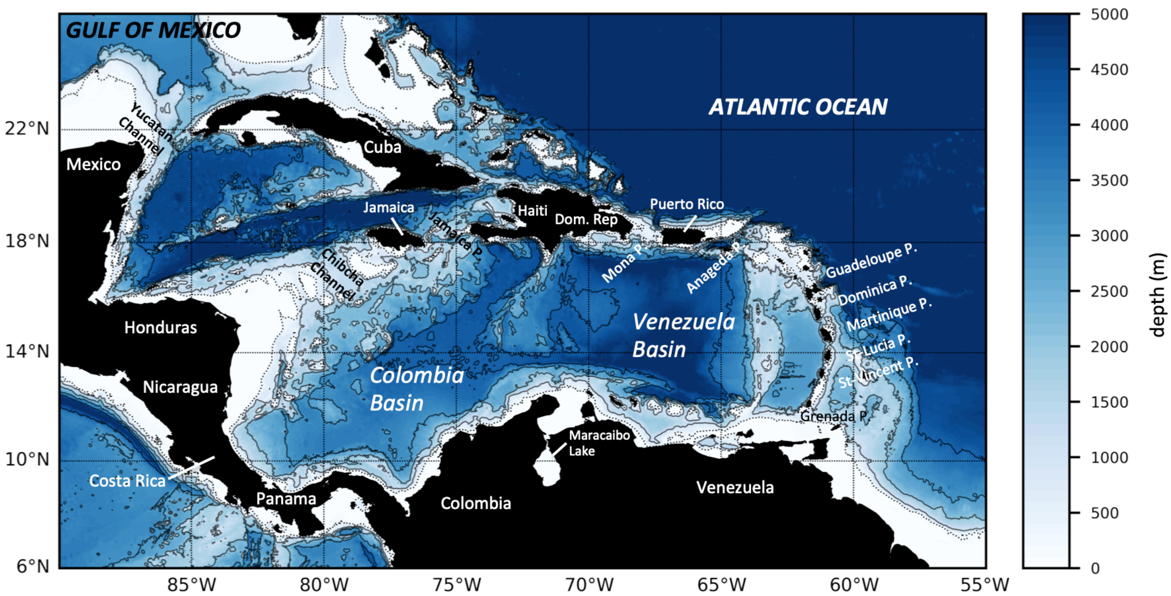

FIGURE 2.3: Bathymetry of the Caribbean Sea, from GEBCO.

2.2.4 Model configuration

The first nest (hereafter NEST32) has a 1/32° horizontal resolution (1:2 grid ratio with the parent), with one day of spinup, and the second nest (hereafter NEST96) has a 1/96° resolution (1:3 grid ratio with its parent, NEST32), with 3 days of spinup. The spinup procedure is represented on Fig.2.4. The parent and children model setup and the model parameters of the experiment are listed in table 2.1.

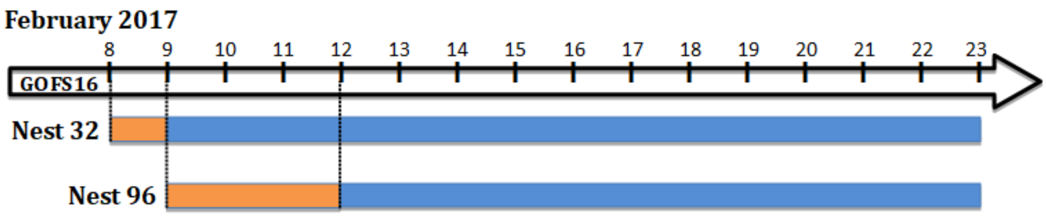

FIGURE 2.4: Spinup procedure. 1 day for the first nest (NEST32), and 3 days for the second nest (NEST96).

The stretched z-coordinate partial step were used for the vertical discretization. Fig.2.5 shows the distribution of the vertical levels for each resolution, according to equation 2.9. The parameters were chosen so the oceanic upper-layer has a submesoscale resolving resolution. The method chosen for the vertical levels depend on the maximum depth of the domain. The maximum depth of the two nesting differ by almost 2000 m, hence the difference between the two curves. As a result, the surface for the second nesting is better resolved.

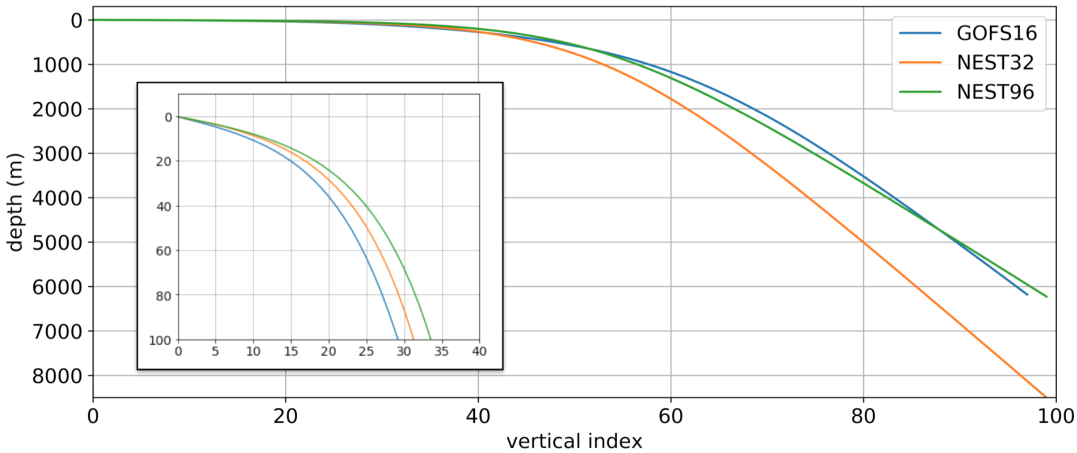

FIGURE 2.5: Distribution of the vertical levels with a focus on the first 100 m (box).

2.3 Datasets and model validation

We describe in this section the datasets used to assess the representativeness of the mesoscale features in the Caribbean Sea seen from the model data GOFS16. Two datasets are used in mean for comparison: the HadISST reconstructed SST data, and satellite data from AVISO for SSH and geotrophic velocities.

	Parent	Nest 1	Nest 2
Time			
Time period	2017.02 08-23	2017.02 09-23	2017.02 12-23
t_{spinup} (days)	–	1	3
time step (s)	200	100	36
Output	daily	hourly	hourly
Spatial grid	**Horizontal grid**		
Δ_x, Δ_y	1/16° $\sim$ 6.8km	1/32° $\sim$ 3.5km	1/96° $\sim$ 1.2km
longitude (°E)	global	[-89.0, -58.0]	[-84.0, -73.0]
latitude (°N)	global	[7.9, 20.525]	[14.0, 18.20312]
$n_x \times n_y$	–	993 × 405	1057 × 405
	Vertical grid		
	z-coordinate with partial step		
n_z	98 h_{sur}=-4068.77 m, h_0=82.4 m h_1=6.815951 m h_{cr}=12.0, h_{th}=30.35101	100 z_{max}=8499.12 m dz_{min}=0.6 m h_{cr}=16.0, h_{th}=55.0	100 z_{max}=6227.62 m dz_{min}=0.6 m h_{cr}=16.0, h_{th}=55.0
Physics	**Horizontal subgrid-scale physics**		
Viscosity coeff.	-0.5×10^9, bilaplacian	-5.0×10^9, bilaplacian	-3.125×10^8, bilaplacian
Diffusivity coeff.	80, laplacian	40, laplacian	20, laplacian
	Vertical subgrid-scale physics		
	TKE mixing	Pacanowski-Philander mixing	
Viscosity coeff.	1.2×10^{-4}	1.2×10^{-5}	1.2×10^{-6}
Diffusivity coeff.	1.2×10^{-5}	1.2×10^{-5}	1.2×10^{-6}
EVC Mix. coeff.	10	10	10
	Model parameters		
Bottom			
	Drag coefficient	1.0×10^{-3}	
	Turbulent KE	$2.5 \times 10^{-3}\mathrm{m}^2/\mathrm{s}^2$	

TABLE 2.1: Parent and children model setup and model parameters of the experiment.

2.3.1 Sea-surface temperature observational data

The HadISST is a monthly global field of SST on a $1^\circ \times 1^\circ$ grid available from 1871 to now. The SST data are taken from the Met Office Marinee Data Bank (MDB). The SST field is reconstructed using an EOF-based technique, the reduced space optimal interpolation (RSOI), followed by superposition of quality-improved *in situ* SSTs from ships and buoys, and bias-ajusted SSTs from the satellite-borne advanced very high resolution radiometer (AVHRR), to restore local details. See Rayner et al. (1966) for more.

2.3.2 Sea-surface heights satellite data

Satellite data can provide a good mean to compare model data with observations, and therefore assess the quality of the model data. In this optic, we use data from AVISO, near-real time L4 sea-surface height and derived variables processed from the DUACS multimissions altimeter data processing system, combining altimeter data from Jason-3, Sentinel-3A, HY-2A, Saral/AltiKa, Cryosat-2, Jason-2, Jason-1, T/P, ENVISAT, GFO and ERS1/2. The product includes sea level anomalies computed with respect to a twenty-year mean, and derived additional variables, such as absolute dynamic topography (ADT) and geostrophic currents.

Chapter 3

Mesoscale variability in the Caribbean Sea

3.1 Model validation

3.1.1 Ocean tracers

The sea-surface temperature of GOFS16 and HadiSST datasets is shown in Fig.3.1. The mean temperature field for GOFS16 is computed over the time period Feb. 8th-23rd, 2017, and the HadiSST is the monthly-mean of February 2017. In general, the model data is a a little bit colder than the observations, but the mesoscale features are similar. The warmer temperature are found in the Colombian basin and towards the Cayman basin, as well as along the meandering Caribbean Current. The Venezuela basin shows to be slightly warmer for the observations, and the along-coast water temperature of northern South America is slightly colder for GOFS16.

The T-S diagrams of model data GOFS16 between Feb. 8th and 23rd, 2017 and of observations taken from CTD stations during the expedition SO164 in the Caribbean Sea, between May 22nd and June 28th, are 2002 displayed in Fig.3.2. It is noteworthy to mention that the observational data were taken in spring, as the model data cover a two weeks period in winter. However, the lack of observations in the Caribbean Sea obliges this comparison. The vertical profile of temperature and salinity, and of the Brunt-Väisälä frequency (N^2) of GOFS16 is shown in Fig. 3.3. The upper layer (60 m) is the relatively fresh water mass Caribbean Water (CW), with salinity around 35.5 psu and lower, and high temperatures of 26-28°C arising from the air-sea heat fluxes. The salinity maximum is attributed to the Subtropical Under Water (SUW), with a salinity of 37 psu. As seen on the vertical profiles, the SUW is located between 150-170 m, and has a temperature of 22-26°C. The salinity minimum of 34.8 psu found around 700 m in the model and 800 m in the observations is the signature of the Antarctic Intermediate Water (AAIW), with temperatures of 4-6°C. In general, there is a good agreement for the deep water branch. It is fresher and slightly warmer in the observations for the upper layer, which can be explained by the offset in season.

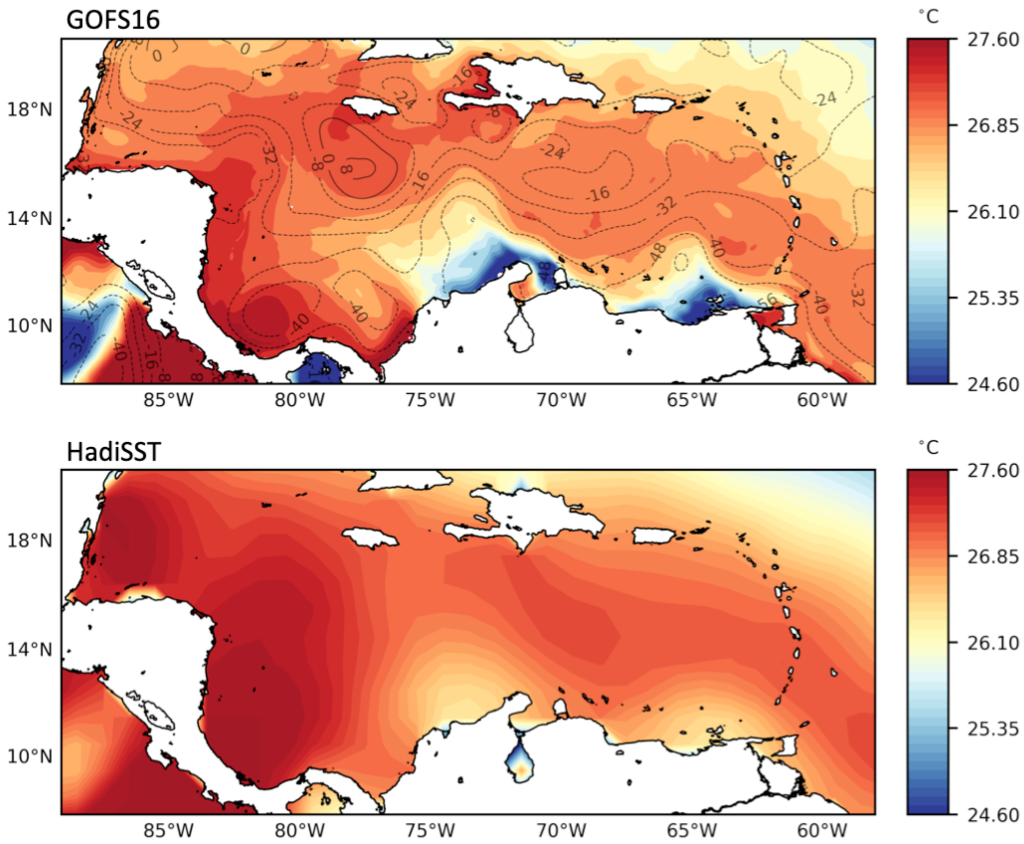

FIGURE 3.1: Time-mean SST of GOFS16 (top) and HadiSST (bottom). The GOFS16 time period is from Feb. 8th-23rd 2017, and HadiSST is the monthly mean of February 2017. The GOFS16 has SSH contours in cm overlayed.

3.1.2 First baroclinic Rossby radius

The first baroclinic Rossby radius of deformation is calculated using the definition from Chelton et al., 1998:

$$\lambda_1 = \frac{1}{f_0 \pi} \int_{-H}^{0} N(z) dz$$

In the Caribbean Sea, the average value for the Coriolis parameter $f \approx 3.6 \times 10^{-5} \mathrm{s}^{-1}$, N^2 varies vertically according to Fig.3.3 on the right panel, reaching down to $H = 5$ km. The first baroclinic Rossby radius was found to be $\lambda_1 = 75$ km, which falls between the range 60-80 km provided by the author. Given that GOFS16 has a horizontal resolution of $1/16°$, which corresponds to 6.8 km in the Caribbean Sea, it is expected that the mesoscale dynamics is well resolved by this dataset, in this region.

3.1.3 Sea-surface height

The general circulation pattern and the presence of mesoscale eddies can be understood based on the SSH shown in Fig.3.1 and 3.4, due to the constraint of the geostrophic balance. In the Colombia basin, the presence of two big cyclonic eddies

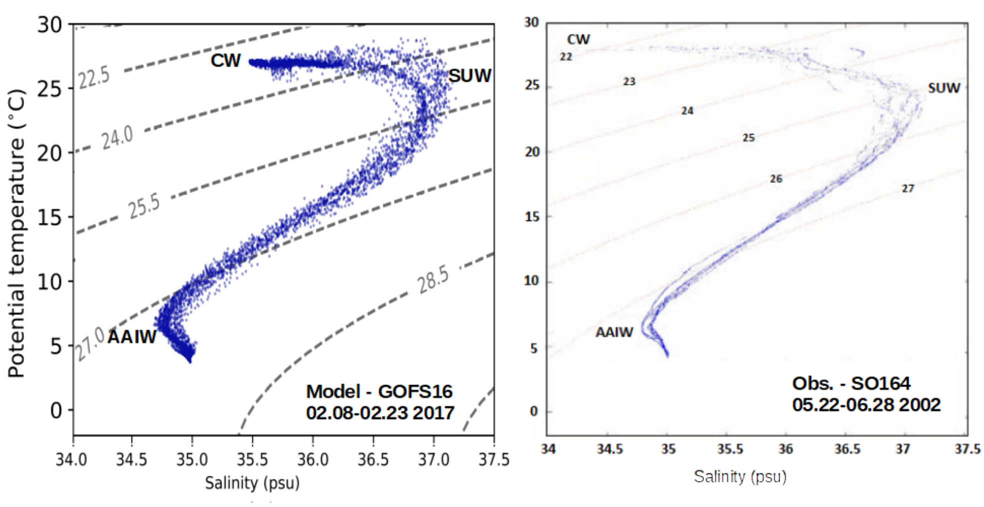

FIGURE 3.2: T-S diagram of (left) model data GOFS16 and (right) observations taken during the SO164 expedition. Note that model data are in winter, as for observation data are in spring.

with centre of ~ -42 cm is clear both in the model data and the observations. These eddies are part of a strong cyclonic circulation, which is referred to as the Panama-Colombia Gyre in Jouanno et al. (2008). Around 70°W below Dominican Republic, where the north Caribbean current flows, GOFS16 shows the existence of a cyclonic eddy with SSH of -6 cm at the centre. It is not clear in GOFS16 if this cyclonic eddy is present. The signature of the south Caribbean current (sCC) clear in the two models, entering the sea in the lower part of the lesser Antilles, joining the north Caribbean current (nCC) around 75°W, then partly entering the Panama-Colombia basin, while the remaining water leaves the Caribbean Sea through the Chibcha Channel. Another interesting feature is the big anticyclonic eddy with center at 78°W and 16°N. Its imprint in the SSH is undeniable in the two models, but GOFS16 exhibits a higher amplitude of the centre (2 cm more).

3.1.4 Geostrophic velocities

We compare the GOFS16 geostrophic velocities to the derived geostrophic velocities from sea-level satellite data. Fig.3.4 shows the time-mean (8-23 Feb) geostrophic velocities of GOFS16 (top) and of satellite data (bottom), with SSH and SLA in colors. Very similar patterns are observed : the boundary current along the northern South American coast, the Panama-Colombia cyclonic gyre composed of two smaller cyclonic circulations, the meandering nCC joining the sCC around 75°W, smaller cyclonic eddies between 65 and 73°W, and finally the strong anticyclonic eddy at 78°W and 16°N. Amplitudes of the velocities also show to be similar. The question whether the anticyclonic eddy is a typical eddy of the Caribbean sea or not remains, but it is at least present in the observations.

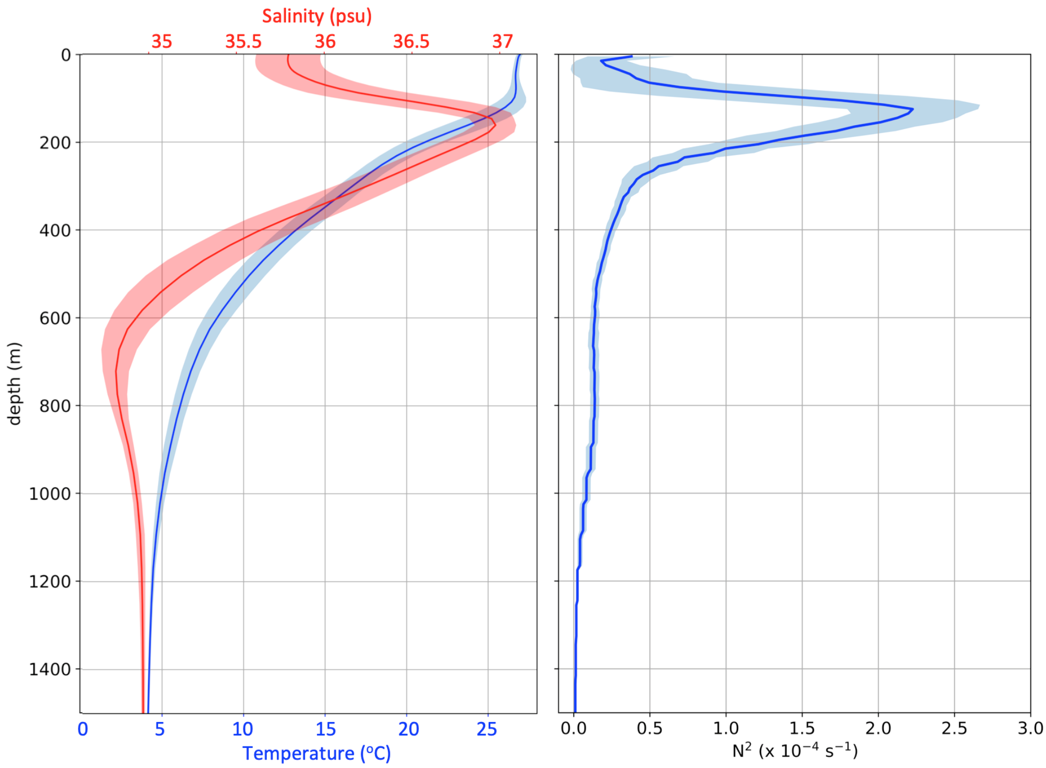

FIGURE 3.3: GOFS16 temperature and salinity vertical profiles (left) and brunt-vaisala frequency N^2 (right).

3.2 Parent model (1/16°)

The parent dataset used for the experiment is the GOFS16 dataset, it has a resolution of 1/16°, which corresponds to 6.3-6.9 km in the Caribbean Sea. The instantaneous map of the total velocity on Feb. 8th is shown in Fig.3.5 shows, at 10 and 150 m depth. The MLD in the Caribbean Sea was found to be around 100 m (Fig.3.6), so we are looking at the velocity field above and below the MLD. The current path near the Lesser Antilles is different for 10 m depth and 150 m depth. At 10m, the flow is dominated by a strong and energetic surface jet flowing through the Grenada Passage. This input to the Caribbean circulation comes from the Brazil current, the narrow poleward return flow of the Subtropical Gyre. At 150 m, the inflow in the central islands is coming from the return flow of the Meridional Overturning Circulation (MOC) from its North Brazil current branch, and enters the Venezuela basin through the St-Lucia Passage. The paths of the circulation vary greatly between 10 m and 150 m depth. In the first case, the main flow follows the South American coast westward and forms the southern Caribbean Current (sCC) by merging with water coming from the Guadeloupe Passage around 66°W. It slightly deflects northward at Maracaibo and continues its way, meandering. One part turns south to join the Panama-Colombia cyclonic gyre, present in the two SSH local minima (Fig.3.1, top figure), and another part joins the anticyclonic eddy located at 77°W-16°N. The water leaves the sea at high speed through the Chibcha channel, still visible at 150 m

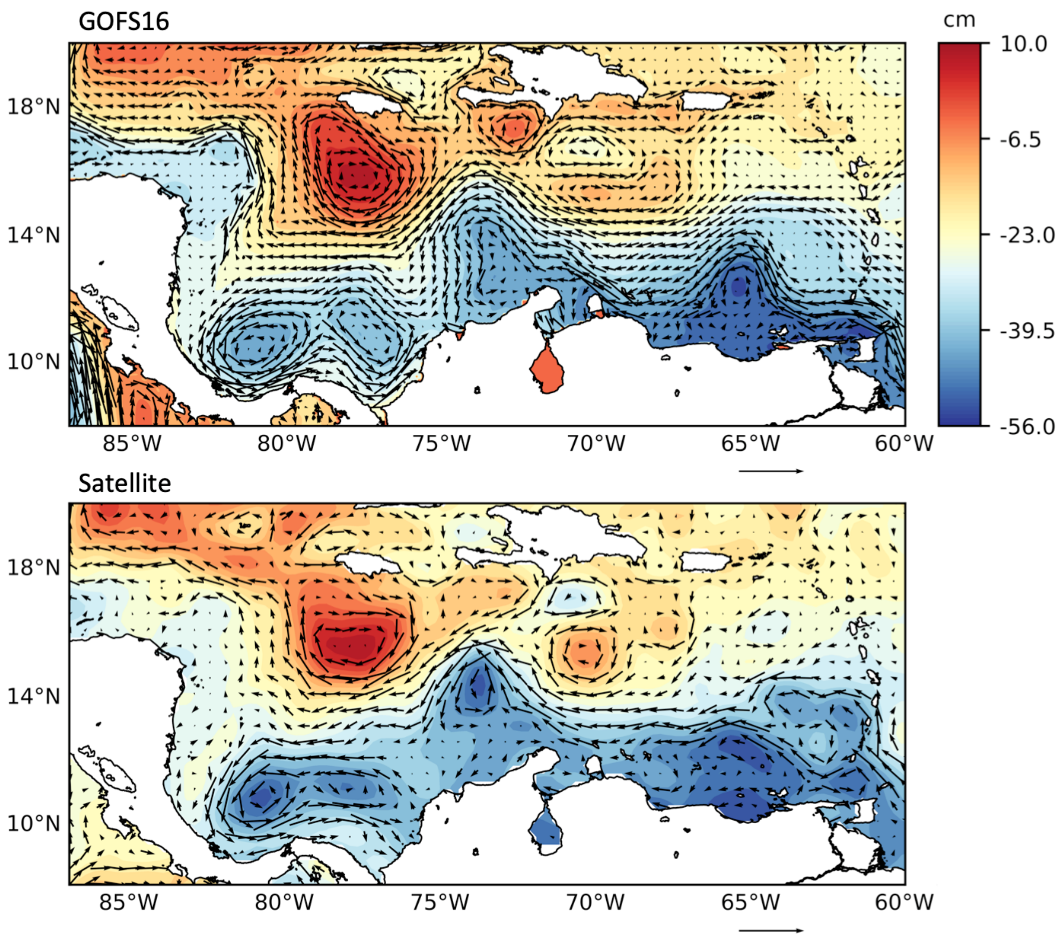

FIGURE 3.4: Mean geostrophic velocities and SSH for (top) GOFS16 and (bottom) satellite data from AVISO. The time-mean is computed over the time period from Feb. 8th to 23rd. The arrow is $1 ms^{-1}$.

depth. At this depth, however, the along-shore current at the South American coast is rather flowing eastward, a result of the water exiting the cyclonic gyre. A striking feature is again the strong anticyclonic eddy still seen at 150 m depth, with swirling speed up to 0.5 ms^{-1}. In general, the Caribbean circulation is highly turbulent and energetic in this time period. The Caribbean Current meanders through the whole basin around the several energetic cyclonic and anticyclonic mesoscale eddies.

The vertical extent of the different currents is examined by looking at the zonal cross-section at 77°W, cutting right through the anticyclonic eddy. Temperature (top), salinity (middle), and zonal velocity (bottom), all with density contours overlayed, are shown in Fig.3.7, on (left panels) Feb. 8th and (right panels) Feb. 22nd. The vertical structure of the zonal flow reveals the following features:

- The Panama-Colombia Gyre is located between the southern shelf at 9°N and 13°N, following where the outcropping of the isopycnals, and is extending down to roughly 200 m, with its core located at 50 m. Both the temperature are only slightly affected, as they become more homogeneous in the upper 50 m, above the MLD, with salinity of 36.2 psu and temperature of 28°C.

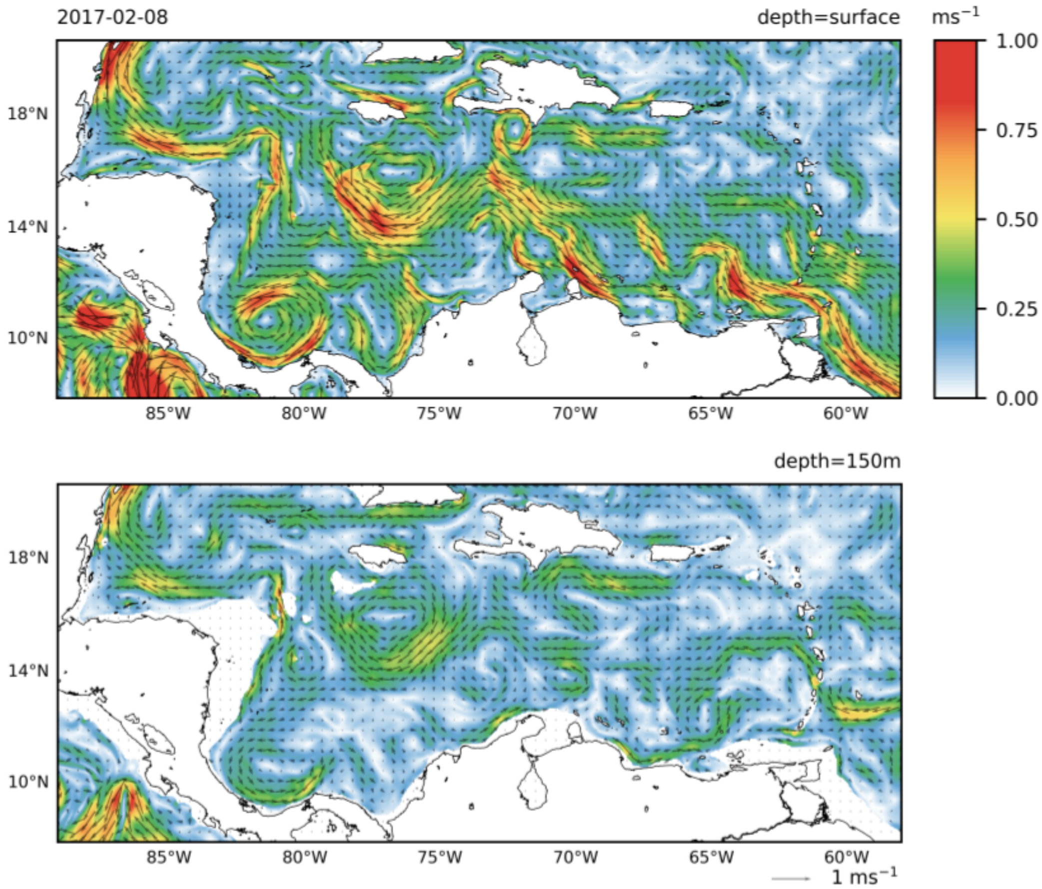

FIGURE 3.5: Velocity field for GOFS16 at the (top) surface (10 m depth) and at (bottom) 150 m depth, on Feb. 8th, 2017.

- The MLD, ranges from 50 m in the cyclonic gyre core to 150 m in the anticyclonic eddy core. At these depths, the temperature is maximum, reaching 28.8°C, and the salinity ranges from 36.6 to 37.6 psu.
- A deep elongated eastward current is located at 13°N, extending from 100 to 1000 m, with its core at 500 m. Probably being part of the Caribbean Coastal Undercurrent, flowing along the South American northern coast.
- The anticyclonic eddy is visible in the zonal velocity structure and outcropping of isopycnals. The core is located about 16°N, it has a vertical extent down to 1000 m, and warmer and fresher water ($\sim$ 35.6 psu). The salinity is greatest at 150 m in the anticyclonic eddy, reaching a value of 37.6 psu.

Between the first and the last day of the present time period, the general features of the mesoscale flow do not show any major changes, except for the internal variability of the currents in the interior. The distribution of the tracers follows the progression of the anticyclonic eddy. From the isopycnals, we can see that the anticyclonic eddy has moved slightly towards the west.

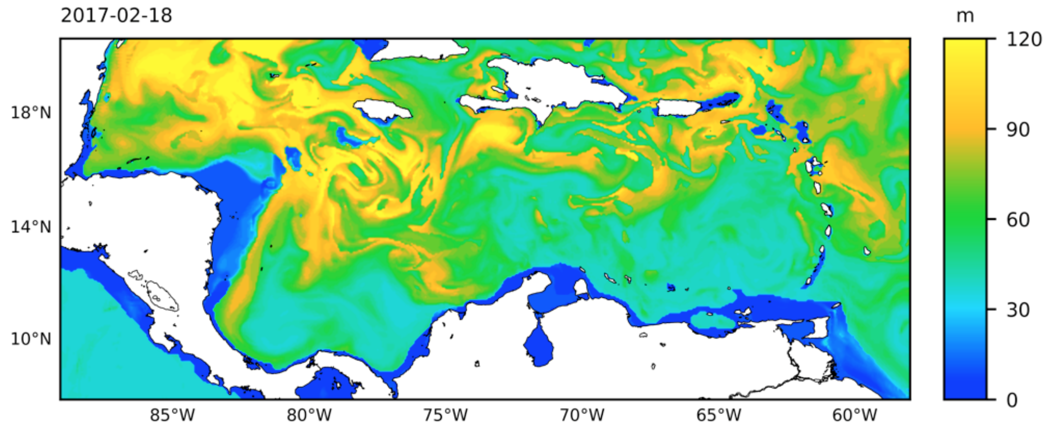

FIGURE 3.6: Mixed-layer depth for GOFS16 on Feb. 8th, 2017.

3.2.1 Anticyclonic eddy

The choice for this two weeks time period was motivated by the presence of the strong anticyclonic eddy located around 77°W-16°N, because the submesoscale structure occurs principally on the periphery of mesoscale eddies (Capet et al., 2008a). From the SST and SSH field daily time-laps of the parent model (Fig.3.8), we can see that within these 14 days, the eddy has moved from approximately 77°W to 78.3°W, giving it a westward propagation speed of roughly 0.12 ms^{-1}, which falls between the given range from observations of 0.02-0.15 ms^{-1} for westward propagating anticyclonic eddies. The temperature and the meridional velocity across the anticyclonic eddy (at 15.6°N) is shown in Fig.3.9, along with the Rossby number field and the velocity field. These plots are snapshots of daily average on Feb. 12th.

Its imprint is marked by the outcropping of $\sigma_\theta = 23$ kgm^{-3}, where the water is warmer than the surrounding water. The SSH reaches a maximum height of 11cm at the center. The temperature is maximum at about 100m depth where it reaches a value of 27.5°C. The meridional velocity cross-section shows that the eddy stretches vertically down to 1000 m. Its latitudinal extent is from 13°N to 17.5°N, giving it a diameter of roughly 500 km, which is also falls into the typical range for mesoscale eddies in the Caribbean Sea, being however considered as a large eddy. Its core, visible from the null velocity values and the SSH field overlaying the Rossby number, is located at about 16°N. The Rossby number is computed from the relative vorticity scaled by f. Since the Coriolis parameter is positive in the northern Hemisphere, positive values of Ro indicate cyclonic circulation (red), and negative values indicate anticyclonic circulation (blue). The correspondence with the velocity field make the direction of the circular motions clearer. The core of the eddy as well as several large horizontal stretches show a clockwise motion, which is what we would expect for an anticyclonic eddy. There are few elongated filaments of cyclonic motions within the eddy and on its periphery. The next step is to increase the resolution and observe if the submesoscale activity has been enhanced.

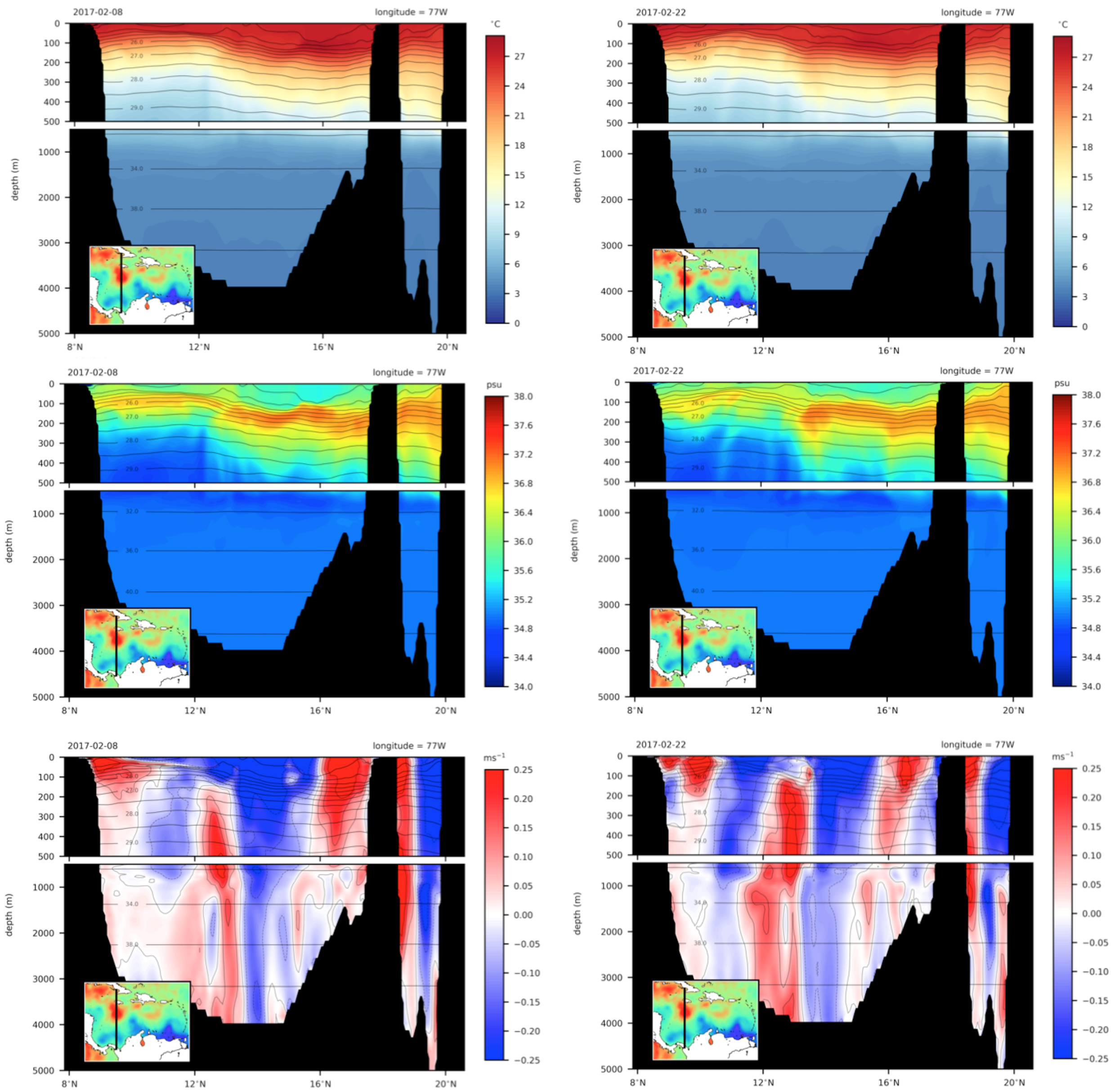

FIGURE 3.7: Cross-section at 77°W of (top) temperature, (middle) salinity and (bottom) zonal velocity, on (left panels) Feb. 8th and (right panels) Feb. 22nd, 2017.

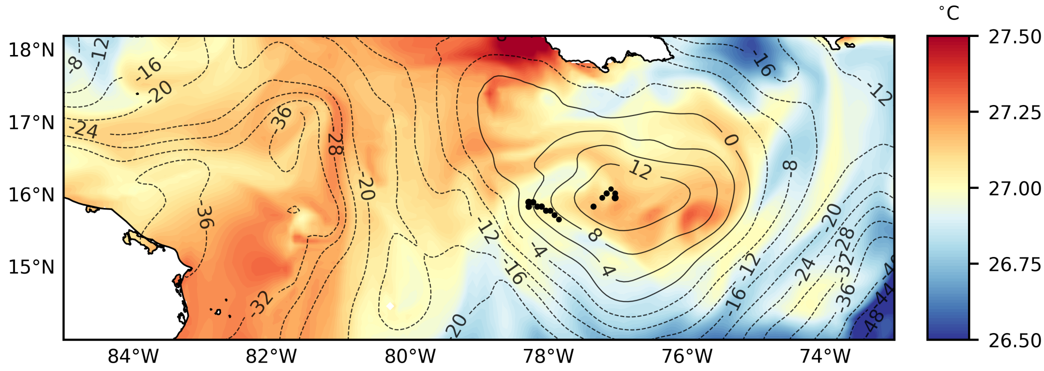

FIGURE 3.8: Westward propagation of the anticyclonic eddy seen from the initial SST and SSH (cm) field. The black dots indicate the position of maximum SSH in time, starting from the left.

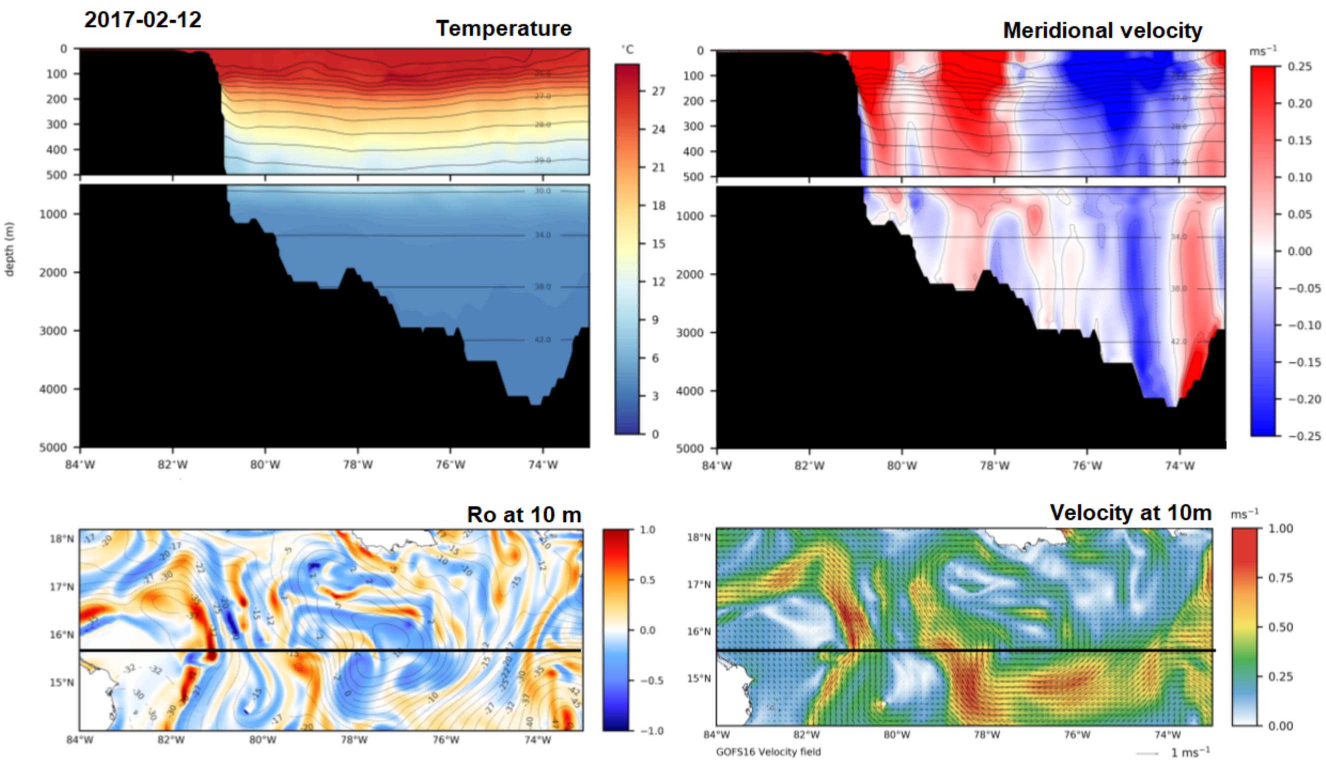

FIGURE 3.9: Snapshots on Feb. 12th of the anticyclonic eddy. On the top panels, temperature (left) and meridional velocity (right) cross-section at 15.6°N. Isopycnals are shown from 23 to 29 kgm^{-3} by 0.5, and from 30 to 42 kgm^{-3} by 4. On the bottom panels, Rossby number (ζ_z/f) with SSH overlayed every 3 cm (left), and velocity field (right). Values for Ro range from -4.44 to 1.72.

Chapter 4

Submesoscale variability

Instabilities tend to form where fronts meet, like at the periphery of mesoscale eddies. At the rim of the anticyclonic eddy found at 16°N and 77°W, enhancement of submesoscale fluctuations through the development of instabilities is expected to be witnessed. To study the emergence of submesoscale dynamics in this area, starting with the parent model at a horizontal resolution of 1/16°, simulations at higher horizontal resolution were done via downscaling. The ratio of the spatial refinement is strongly recommended to be less than 5 to avoid reproducing unrealistic dynamics, so in the present study the ratios were kept at 1:2 and 1:3. The first nesting has a horizontal resolution of 1/32° ($\sim$ 3.5 km) and comprises the whole Caribbean Sea. The second nesting, embedded within the first nesting, has a horizontal resolution of 1/96° ($\sim$ 1.2 km) and fully encloses the anticyclonic eddy.

A hint to the effect of horizontal resolution on temperature is displayed in Fig.4.1, showing the instantaneous SST on Feb. 19th, for the 1/16°, 1/32°and 1/96°resolutions overlayed. In this chapter, results from the effect of horizontal resolution on ocean tracers and ocean dynamics in the Caribbean Sea is presented, with a focus on a smaller region at the rim of the anticyclonic eddy in the last section.

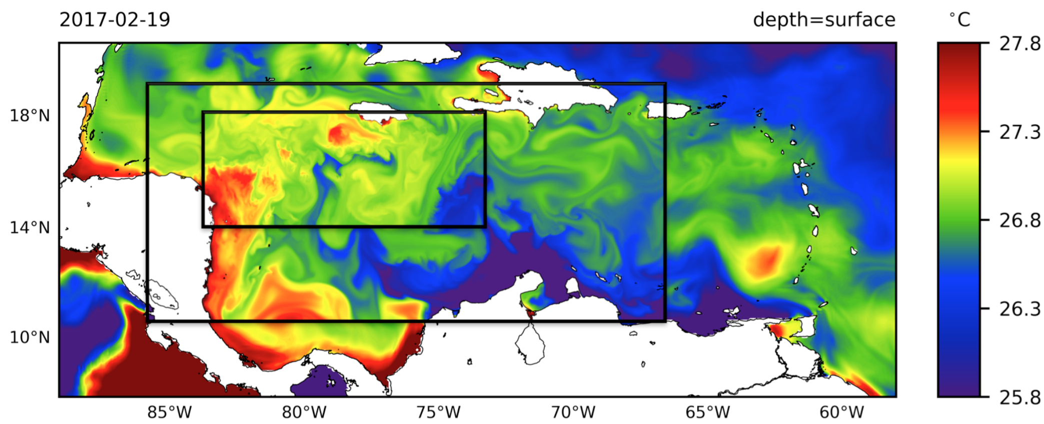

FIGURE 4.1: Instantaneous SST on Feb. 19th. The simulations with resolution 1/16°, 1/32° and 1/96° are overlayed, corresponding to 6.8, 3.5 and 1.2 km, respectively.

4.1 General characteristics

4.1.1 Effects of submesoscale on ocean tracers

The effect of horizontal resolution on sea-surface temperature is shown in Fig.4.2. The resolution increases from top to bottom panels. The NEST32 and NEST96 are daily averages of the hourly outputs.

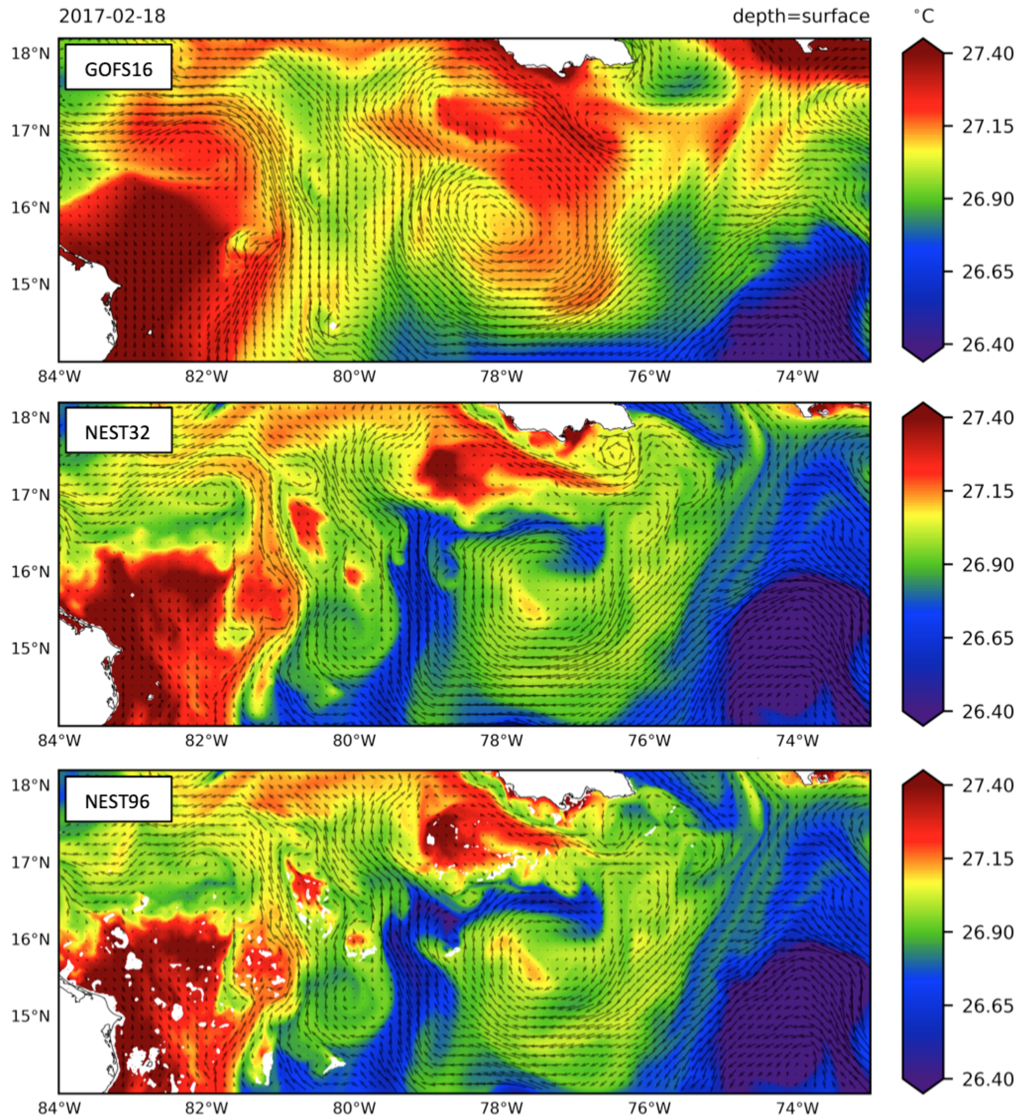

FIGURE 4.2: Sea-surface temperature with velocity field at 10 m depth overlayed, on Feb. 18th for GOFS16 (top), NEST32 (middle), and NEST96 (bottom). NEST32 and NEST96 are daily averages of hourly outputs.

The coherence among the resolutions is high, and the dominant mesoscale patterns across all solutions is still visible. The smaller grid resolution permitted the emergence of an additional structural complexity at smaller scale. Temperature gradients are enhanced for higher resolution, a feature recognizable from filaments emerging and getting thinner. These gradients in temperature are prevalent at the edge of the mesoscale anticyclonic eddy, where submesoscale wiggles in temperature are also observed. The difference in structure is larger between GOFS16 and NEST32, than between NEST32 and NEST96. Between the coarser resolution and the intermediate one, the difference is marked by the emergence of temperature fronts at the edge of the eddy, and an intrusion of a filament of colder temperature within the eddy. The highest horizontal resolution differs from the intermediate one by the presence of even smaller features and thinner fronts, but the general picture is somewhat very similar.

4.1.2 Vorticity and vortical asymmetry

The degree to which the presence of submesoscale instabilities in the anticyclone eddy can be determined is by looking at the surface relative vorticity ζ_z, since through vertical vortex stretching induced by frontogenesis, strong relative vorticity is generated within the mesoscale (Brannigan et al., 2017; Capet et al., 2008b). The Rossby number (Ro$= \zeta_z/f$) at 10 m is shown in Fig.4.3 for all resolutions, on Feb. 18th.

The presence of the anticyclonic eddy is highlighted by the positive SSH contour lines, in all resolutions. At 6.8 km resolution (top panel), the GOFS16 simulation, Ro is mainly within the geostrophic range, between -1 and 1, arguing for little to no evidence for submesoscale instabilities occurring at the periphery of the anticyclone. There is a large and long filament of cyclonic vorticity (Ro $\sim$ 1) around 79.5°W, wrapping itself around the large eddy. Filaments of negative vorticity values are not observed. For the 3.5 km resolution (middle panel), filaments of large Rossby number values ($|$Ro$|$>1), both positive and negative, start to develop at the edge of the eddy, and across the Chibcha channel. This is indicative of a transition to a more ageostrophic regime. The submesoscale flows have relatively small Rossby numbers ($|$Ro$| < 3$), but still a large geostrophic component and thus an imprint into the SSH. The 1.2 km resolution shows a coherent picture with the mid-resolution experiment. Nonetheless, it also reveals much stronger variability in the relative vorticity field at the submesoscales ($\sim$ 10 km), consisting of several small-scale vortices as well as thinner filaments of larger Rossby number. The width of the filaments decreases with each increase in resolution, as it was observed in Brannigan et al. (2017). Overall, for the three resolutions, the filaments are mostly of positive vorticity, and the vorticity is generally smaller towards the centre of the eddy.

The surface relative vorticity shows an increase of ageostrophic flows associated with an increase in horizontal resolution. As seen in Fig.4.4, the relative vorticity field at 800 m at 1.2 km resolution, these changes are not even across depths. Compared to the surface relative vorticity field (Fig.4.3 bottom), the 800 m has a less vortical intensity, resembling that of the 6.8 km resolution. Filaments are thicker and the mesoscale patterns are more heterogeneous. The few very strong vortices that still remain are all located at boundaries. Boundaries are efficient sources of strong vorticity. The difference in regime between depths demonstrates that submesoscale

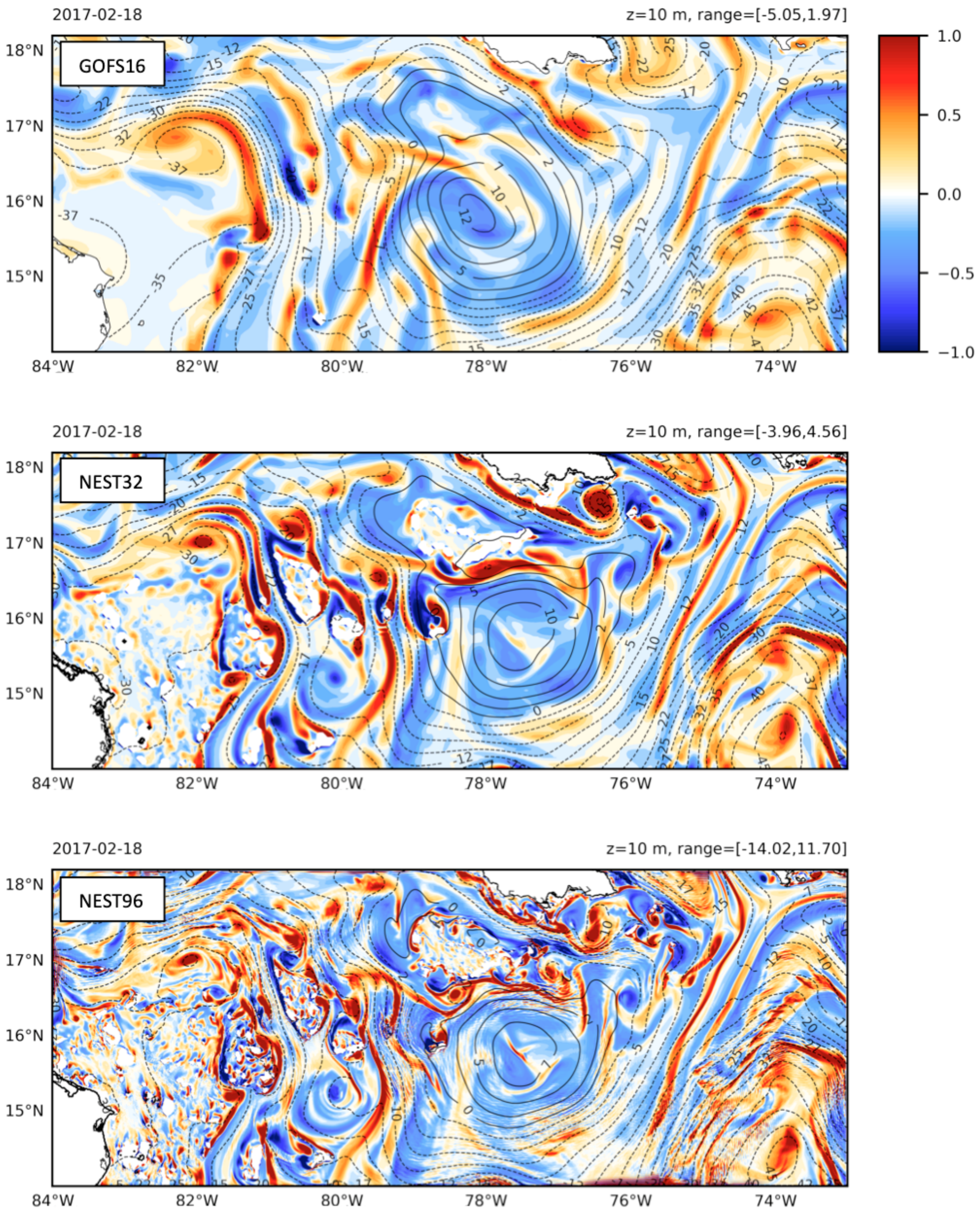

FIGURE 4.3: Rossby number (ζ_z/f) at 10 m depth, on Feb. 18th, for GOFS16 (top), NEST32 (middle) and NEST96 (bottom).

activity seems to be concentrated at the surface. To sum up, the coarse resolution flow is mostly geostrophic, dominated by the Coriolis acceleration. The higher horizontal resolution simulations exhibit large Rossby numbers at the surface. Thus, we expect the submesoscale flows to be significantly ageostrophic in the upper layers, and close to geostrophy in the ocean interior.

The difference in properties between the ocean surface and the ocean interior can be studied when looking at the vertical profile of dynamical quantities such as the kinetic energy (Fig.4.5, left). The profile is an averaged over the area delimited

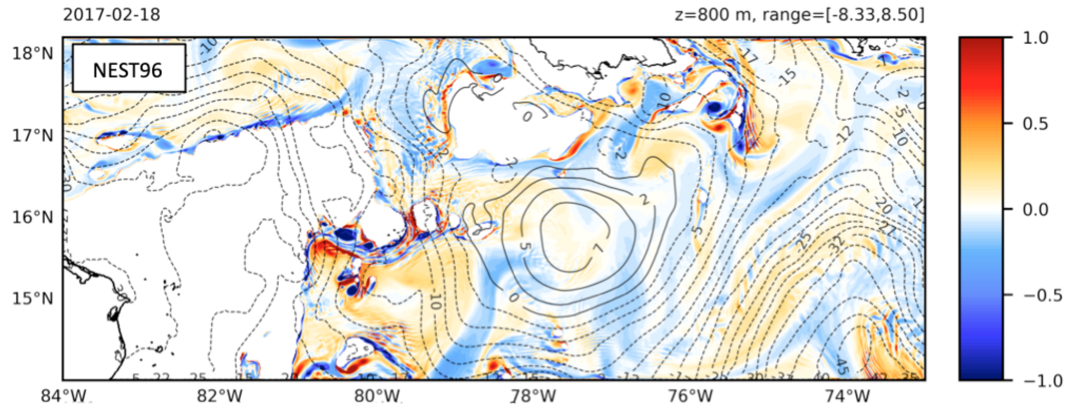

FIGURE 4.4: Relative vorticity at 800 m depth for NEST96 on Feb. 18th, with SSH (cm) contours. Daily average of hourly output.

by 78.4-78.2°W and 15.8-16.4°N. For all resolutions, the kinetic energy is trapped within the first 800 m, but GOFS16 kinetic energy goes faster towards zero, than the two other solutions. The energy is highest within the surface layer, with most of it trapped within the first 100 m. An increase in surface kinetic energy associated with an increase in horizontal resolution is observed, in this area of the size of submesoscale. At the surface, the kinetic energy is greatest at 1.2 km resolution, sign of strong submesoscale activity. On the right panel of this figure, the vertical profile of the Brunt-Väisälä frequency (N^2) shows stronger stratification at the ML base, dominated by GOFS16. Within the ML, between 50 and 100 m, stratification increases with horizontal resolution. The increase in stratification in the surface layer is compensated by a destratification at the ML base.

The first baroclinic Rossby radius of deformation was computed for the three resolutions using the averaged of the N^2 vertical profile, and was found to be 75 km in all cases.

The distribution of the surface vorticity (Fig.4.6) indicates that the horizontal resolution does impact the nature of the flow. In the three cases, the mean total Rossby number is negative (top panel), and the distributions exhibit a vortical asymmetry, expressed by the positive skewness. The GOFS16 simulation already has values of $|\mathrm{Ro}|>1$, meaning that the flow also exhibits an ageostrophic component. The mean Rossby number and skewness listed in the following table:

	GOFS16	NEST32	NEST96
Mean	-0.1	-0.06	-0.04
Skewness	0.67	0.52	0.56

The skewness values are rather small, and the positive tail is thick. No trends for neither the vorticity nor the skewness can be concluded. The vorticity range expands as the horizontal resolution increases. The submesoscale transition is perhaps more evident from the Rossby number mean time series. The positive (cyclonic) mean

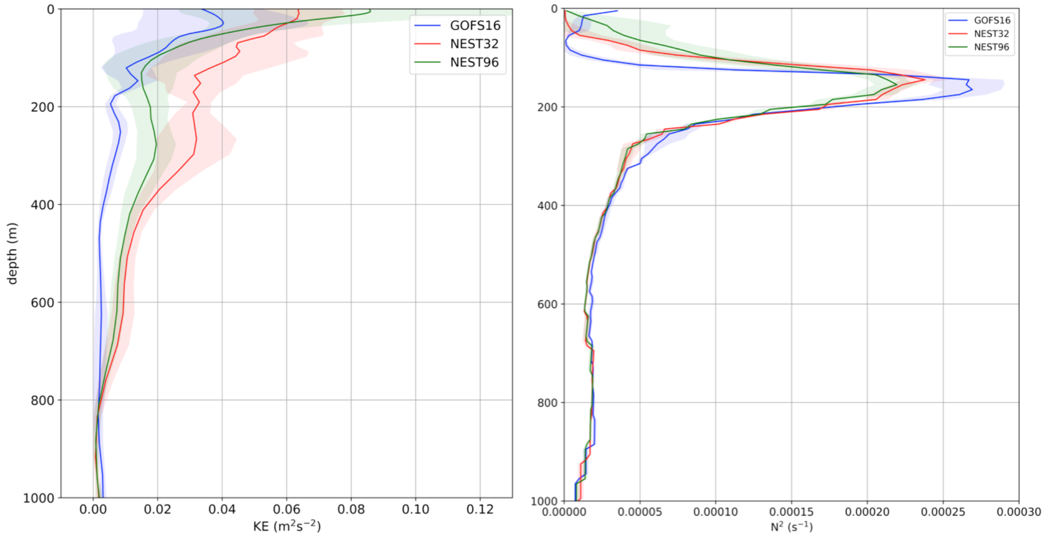

FIGURE 4.5: Vertical profile of kinetic energy (m^2s^{-2}) and Brunt-Väisälä frequency (s^{-1}) for GOFS16 (blue), NEST32 (red) and NEST96 (green), on Feb. 18th, averaged over the area between 78.4-78.2°W and 15.8-16.4°N.

time series is shown on the bottom left, and the negative (anticyclonic) mean time series on the bottom right. The different resolutions start at different days according to their spin-up initialization. NEST32 shows a significant transition to submesoscale of 6 days, where both cyclonic and anticyclonic means grow almost linearly until it stabilizes. The NEST96 vorticity range grows for the first 2 days, time needed to adapt to the new grid, then joins the NEST32 curve. The cyclonic vorticity mean is always larger than the anticyclonic mean.

Overall, the difference in vorticity is more striking between the GOFS16 and the NEST32 experiments, than between the NEST32 and the NEST96 experiments. The NEST96 experiment seems to be more a refined version of the NEST32 rather than showing additional features only permitted at this resolution. Neverteless, it is evident that the passage between the 1/16° and the 1/32° allows submesoscale eddies to develop in the Caribbean Sea. It is important to note that the increase in resolution also brings the emergence of several islands as well a refined bathymetry which could also have an impact on the flow structure.

4.1.3 Energy spectra

The power spectrum of kinetic energy (KE) is used to characterize the energy distribution in terms of lengthscales. In Fig.4.7 is shown the KE spectrum on the last day of the simulation, over the whole area covered by NEST96, at 0, 100 and 400 m depth. The KE spectra were computed following Klein et al. (2007). They are mean spectra calculated over boxes of 2°×2° where no NaN values were found. Considering

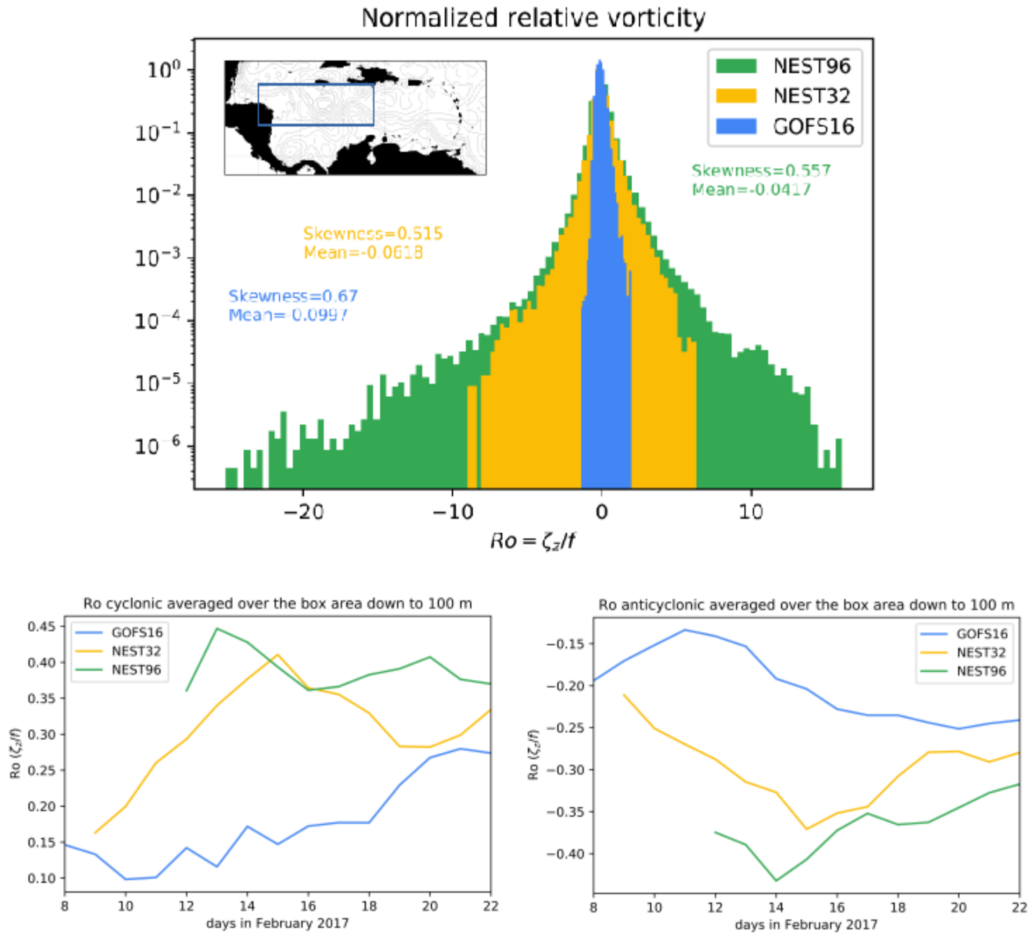

FIGURE 4.6: Surface relative vorticity (scaled by f) distribution and mean time-evolution, over the area enclosed in the box.

that an increase in resolution refines the bathymetry, therefore bringing more boundaries within the domains, the number of boxes might differ per resolutions and per depth. The values are detrended, and a Hanning window is applied to the 2D fields prior computation of the Fast Fourier Transform (FFT). The Power Spectrum Density (PDS) is found by integrating the FFT over the radial wavelength numbers. For the visual matters, the wavelengths (km^{-1}) are transformed into lengthscales (km), in order to facilitate the lecture between the different regimes. The KE spectrum computed from the geostrophic velocities (themselves computed from the SSH) is also shown, as well as the barotropic KE spectrum (except for GOFS16 because some elements were missing in order to compute the barotropic velocities). Also displayed are the -4 (full line) and -5/3 (dotted line) theoretical curves.

The surface flow is showing different behaviours depending on the resolution. The surface flow of GOFS16 is in accordance with the SSH spectrum, confirming the geostrophic equilibrium mentioned earlier for GOFS16. In the case of NEST32, the difference varies among the length scales. The surface flow is closer to geostrophy at large length scales, and the smaller scales become more energetic, starting from

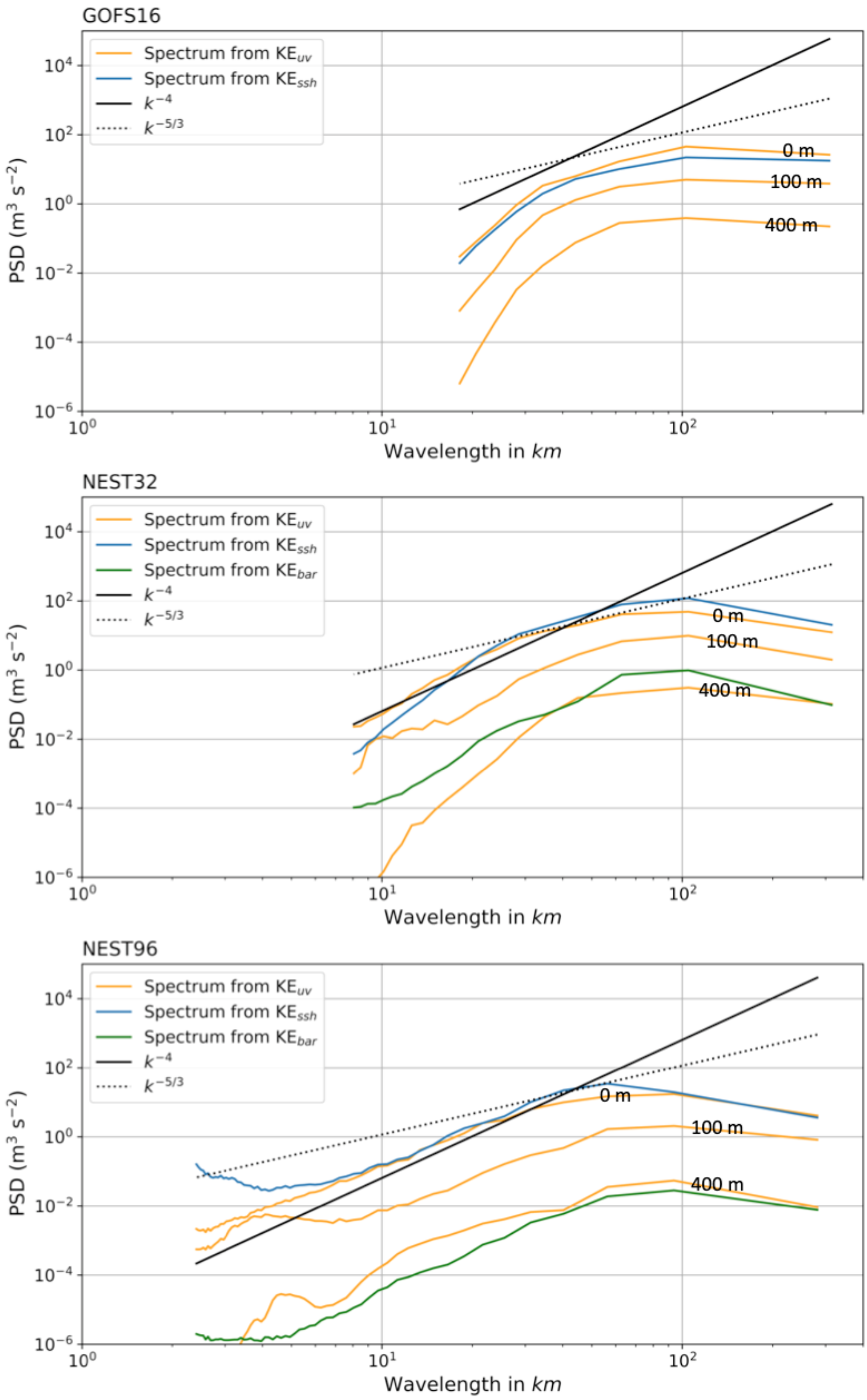

FIGURE 4.7: Kinetic energy spectra (km) of GOFS16, (middle) NEST32, and (bottom) NEST96, at 0, 100 and 400 m depth. The blue curve is the KE spectrum estimated from the SSH, the orange curve from the total velocities, and the green curve from the baroclinic velocities. The theoretical lines of $k^{-5/3}$ (dotted) and k^{-4} (black) are displayed for comparison.

20 km, showing that more energy is put into the ageostrophic component. NEST96 surface KE spectrum follows the geostrophic one until 8 km length scale, where the geostrophic flow component experience a sudden increase in energy.

The KE spectra exhibit significant differences between the different depths. For GOFS16, the spectra monotonically decrease in energy with depth, keeping however a constant value for large scales, then following the $k^{-5/3}$ from 100 to60 km, then steepening. The KE spectra of NEST32 have less energy with depth. At 400 m, the KE spectrum is lower than that estimated from the barotropic velocities. The surface flow of NEST96 is shallow ($\approx k^{-4}$) for a large spectral band, highlighting the strong energy in the small scales at the surface. As the depth increases, the smaller wavelength bands have steeper spectra, implying less energy in the smaller scales. The deep flows for NEST32 and NEST96 are close to the barotropic ones, suggesting that the energy is mostly captured by this mode at great depths.

In terms of spectral bands, GOFS16 has more energy concentrated in the lengthscales >10^2 km, than for the two nestings, at the surface. There is more energy in the geostrophic component in NEST32 than GOFS16, in general. For lengthscales between 50-100 km, NEST32 is more energetic, and NEST96 is the least energetic. Between 10-50 km, a similar behaviour is observed. The fluctuations towards smaller scales (< 10 km) for NEST96 could be attributable to the presence of noise within the simulation.

4.1.4 Effect on the anticyclonic eddy

The increase in horizontal resolutions appears to affect the dynamics of the anticyclonic eddy. The SSH value at its centre as well as its westward propagating velocity are both lessened when increasing the resolution. Between between Feb 12th and 23rd, the westward velocity of the eddy was 0.12 ms^{-1} for GOFS16, 0.08 ms^{-1} for NEST32, 0.11 ms^{-1} for NEST96, and the maximum SSH value, corresponding to the centre of the eddy, decreases with resolution (Fig.4.8). After 5 days of simulation with NEST32, the centre of the eddy always stays lower than that of GOFS16, with a difference of 1-2 cm. The center of the eddy in the NEST96 simulation keeps decreasing after the first day of simulation, first following its parent model NEST32, then continues on a decreasing evolution contrary to NEST32 from its 4th day of simulation. On Feb. 22nd, the difference between GOFS16 and NEST32 is 3 cm, and between NEST32 and NEST96 4.5 cm.

4.2 Case study: rim of the anticyclonic eddy

This section focuses the analysis on a smaller domain, at the rim of the anticyclonic eddy (Fig.4.9), into which the submesoscale processes are more clearly depicted. The results presented in this section are based on the $1/32°$ resolution (3.5 km). The $1/96°$ resolution is discarded here because the significant presence of numerical

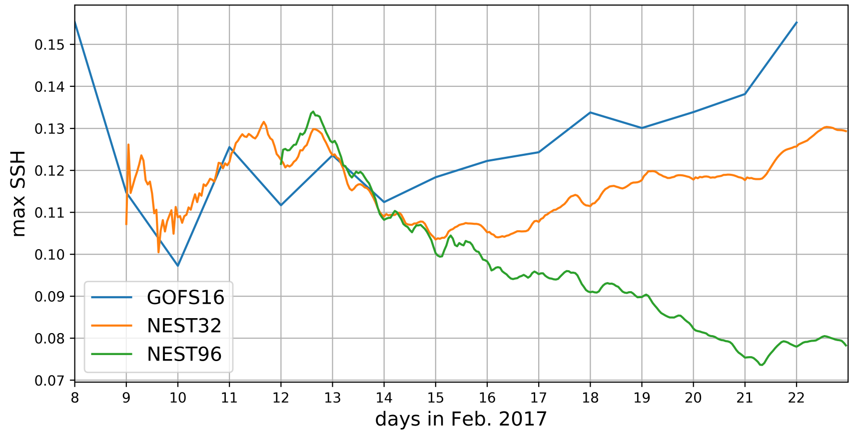

FIGURE 4.8: Time series of the maximum value of SSH (m) corresponding to the centre of the anticyclonic eddy.

noise in the simulations could possibly be an initiator of spurious submesoscale features. For the following section, the geography of the chosen area will be described, and the event of the shedding of a submesoscale eddy is investigated through some dynamical variables in order to understand the response of the background oceanic state to the submesoscale eddy permitting grid.

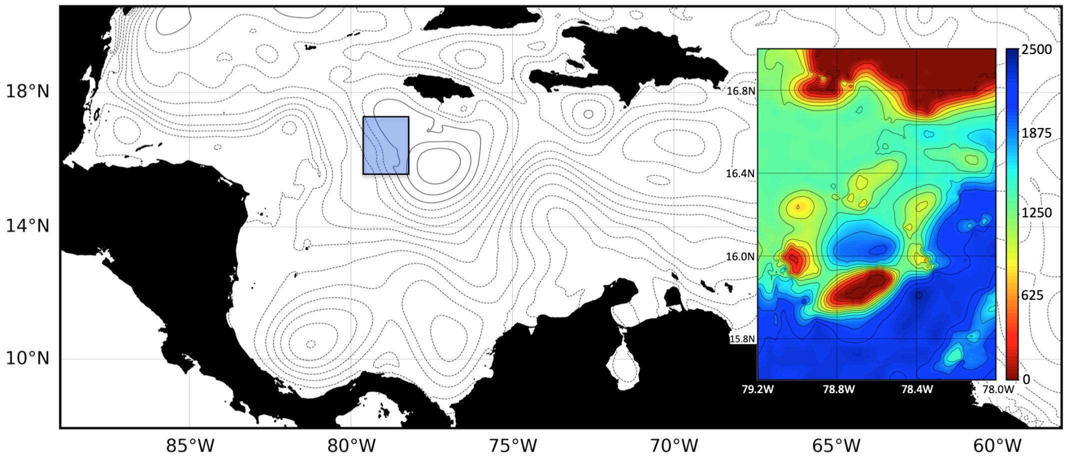

FIGURE 4.9: The domain of analysis of this section is located at the rim of the anticyclonic eddy (hatched box). The bathymetry of the small domain, from GEBCO, is shown on the right. Contours are made every 200 m, and colors are from 0 (red) to 2500 m (blue).

The domain ranges from 79.2 to 78.0°W, and from 15.4 to 17.0°N, corresponding to a 130×180 km box. The choice of the area is motivated by the strong localized blooming of submesoscale activity, as seen from the Rossby number and the velocity fields in the previous sections. From the bathymetry map, using the data from GEBCO, we note the presence of two islands between 15.6 and 16°N, and a major drop down to 2500 m deep in the south of these islands. Above the islands, the ocean floor is shallower (about 1000 m) but still not entirely uneven.

Between Feb. 15th and 22nd occurred the shedding of a submesoscale eddy at

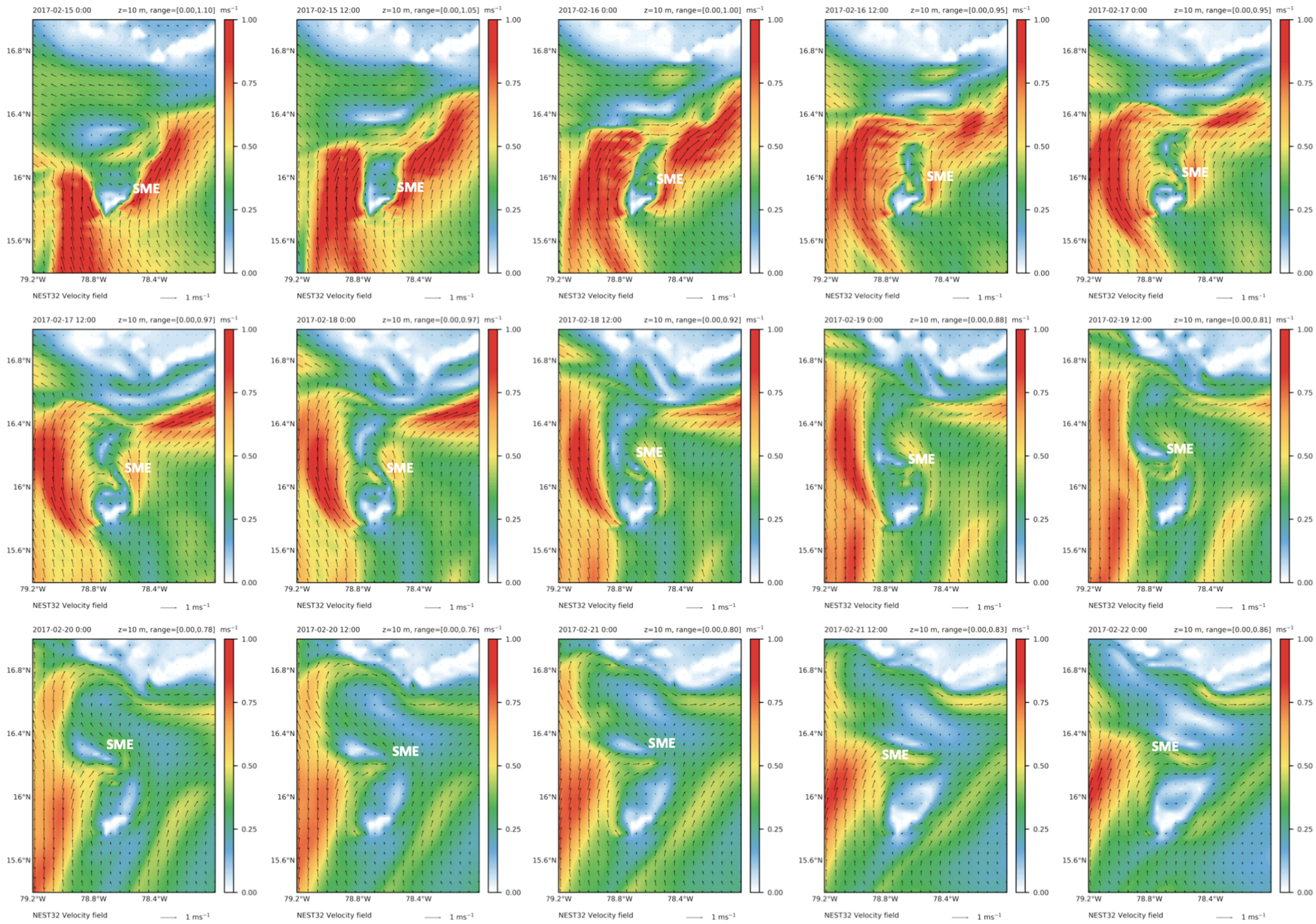

FIGURE 4.10: Shedding of a submesoscale eddy seen from the velocity field at 10 m depth at 3.5 km resolution. Time period is from Feb. 15th to 22nd, shown every 12h from hourly outputs.

the rim of the anticyclonic eddy (Fig.4.10). The event is presented from hourly snapshots every 12h from the beginning, at 10 m depth. The northeastward velocity on the right side of the domain is attributable to the large anticyclonic eddy. Around 78.7°W and 15.8°N, at the southern tip of the biggest island of this small domain, there is a separation of the incoming flow with velocity of 0.5 ms^{-1}. A submesoscale eddy (SME) of cyclonic vorticity starts to form on Feb. 15th. The SME becomes a clear ring from the next day, and propagates along the anticyclonic eddy current, northward, then joins in the branch of the eddy, and merges with it (not shown). It has a diameter of roughly 7 km, which falls within the submesoscale range.

Fig.4.11 shows the density, horizontal velocity, vertical velocity, Rossby number, strain rate, and temperature on Feb. 18th, when the SME is most visible. The SME arises from the interaction between the oceanic flow and the island, as it occurs in the case of topographic wakes. The incoming flow is induced high positive vorticity (Ro=3.77) at the contact with the boundary (Fig.4.11 d)), and its counter part with a high negative vorticity (Ro=-3.44). The lateral strain rate is also large at this location, and strong negative vertical velocities (downward) are following the movement of the SME. Other interesting features are that its imprint on the SSH is visible, meaning that it is not merely ageostrophic. Moreover, temperatures at the SME are slightly colder than the surrounding, perhaps related to the cyclonicity of the motion.

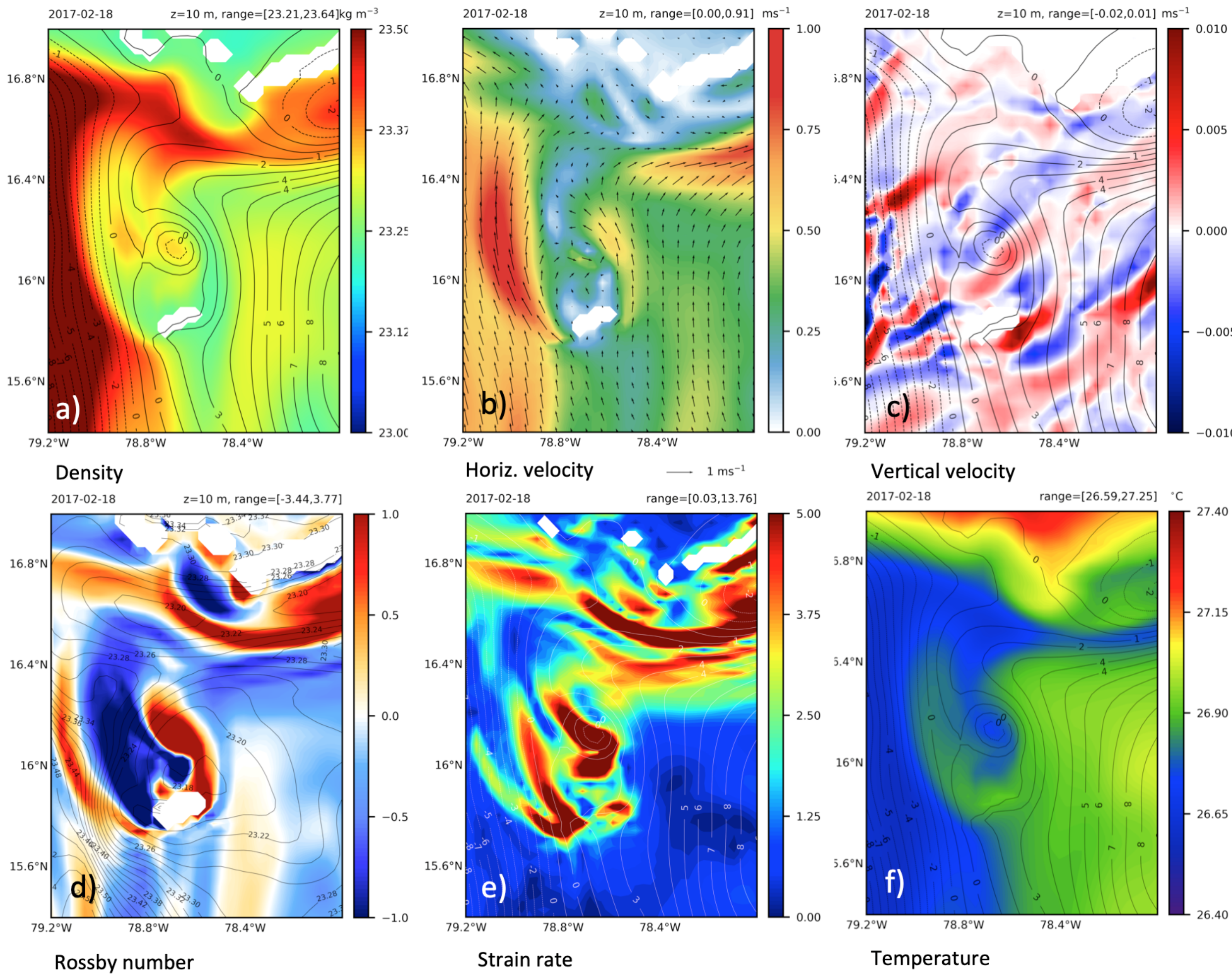

FIGURE 4.11: Rim of the large anticyclonic eddy, at 1/32°resolution ($\sim$ 3.5 km). Daily average of hourly outputs. At 10 m depth: a) density, b) horizontal velocity, c) vertical velocity, d) Rossby number (ζ_z/f), e) Strain rate, and f) sea surface temperature. Black contours show the SSH, expect for Ro where it shows the density.

The time-evolution of the Brunt-Väisälä frequency (N^2) is shown in Fig.4.12, for GOFS16 and NEST32 for means of comparison. The average is made over the small black box shown in the bottom right corner. Day 1 corresponds to Feb. 9th, day 6 to Feb. 14th, and day 12 to Feb. 20th. In these 12 days, for both cases, the maximum value located at the MLD increases of 0.8×10^{-4} s^{-2}. The position of the maximum increases slightly from 180 m to 170 m. The day 6 curve moved of 0.5×10^{-4} s^{-2} for GOFS16 and of 0.3×10^{-4} s^{-2} for NEST32, with respect to the first day. Overall, there is an increase in stratification at the ML base, and a small decrease (0.5-1$\times 10^{-4}$ s^{-2}) in the upper ML, for GOFS16 and NEST32.

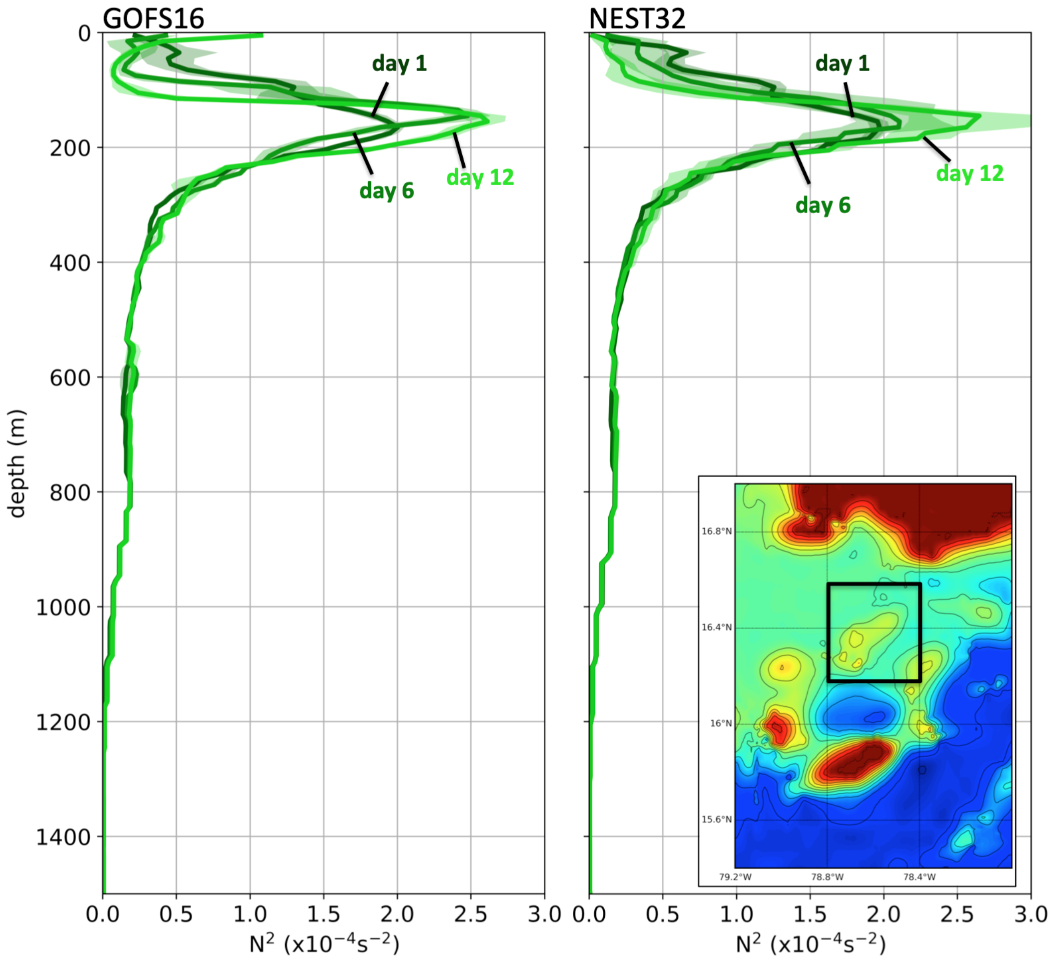

FIGURE 4.12: Brunt-Väisälä frequency (N^2) vertical profile at 3 different days for GOFS16 (left) and NEST32 (right), averaged at the location where a submesoscale eddy passes through (black box).

Chapter 5

Discussion and conclusion

5.1 Discussion of the results

This thesis explored the impact of the horizontal resolution on the ocean dynamics in the Caribbean Sea, for a two-weeks period in February 2017. The mesoscale and submesoscale motions with their respective characteristics were studied through simulations at different resolutions, permitting or not submesoscales. The simulations were carried out using the one-way nesting numerical platform SURF, for the time period Feb. 8-23rd, 2017. The first nesting (1/32°, 3.5 km) comprised the whole basin, while the second nesting (1/96°, 1.2 km), embedded within the first nesting, covered an anticyclonic eddy and about.

In chapter 3, the mesoscale variability in the Caribbean Sea was studied using the GOFS16 data, which has a horizontal resolution of 1/16°, corresponding to 6.8 km in the Caribbean Sea. This region, special for being a semi-enclosed sea with a highly variable bathymetry, has its waters mainly composed of the warm Caribbean Water with (T, S)=(27°C, 35.5 psu), the saline Subtropical Water with (T, S)=(23°C, 37 psu), and the deep fresh and cold Antarctic Intermediate Water (T, S)=(5°C, 34.8 psu). The water flows across the whole basin via the meandering Caribbean Current composed of two branches. The northern branch comes from the Subtropical Gyre which enters the basin through the Mona and the Anageda Passages, and the southern branch comes from the North Brazil Current and the North Equatorial Current entering via the Lesser Antilles islands, follows the South American coast, then splits as one part goes into the Panama-Colombia gyre, and the other merges with the northern branch. The two branches merged together leave the basin through the Chibcha channel, and flow out to the Gulf of Mexico. The GOFS16 instantaneous map of surface velocities showed a very energetic eddying ocean dynamics. Down to 150 m, strong velocities still remained, especially the signature of a large anticyclonic eddy located at 78°W-16°N. This eddy, visible from the outcropping isopycnals corresponding to σ_θ = 23.0 kgm^{-3} at the surface, extends down to 1000 m, and has a warmer and fresher core than the surroundings. The MLD at its location reaches >120 m, where usually it is around 30-60 m in the Caribbean Sea. This eddy is propagating westward with a speed of 0.12 ms^{-1}. With a diameter of 500 km, this anticyclonic eddy is considered large, but all its characteristics falls between the normal ranges for westward propagating anticyclonic eddies in the Caribbean Sea. The first baroclinic Rossby radius of deformation was found to be 75 km, meaning that below this, instabilities in the flow lead to a departure from geostrophy.

Instabilities tend to form at fronts, like at the periphery of an eddy. In this optic, the results presented in chapter 4 were focusing on the area where the large anticyclonic eddy was evolving. The impact on ocean tracers, ocean dynamics, and the vertical of these effects were studied. The main questions are answered in what follows.

1. *What horizontal resolutions is needed for submesoscale motions to develop?*

   While the 6.8 km resolution model very well represented the mesoscale dynamics of the Caribbean Sea, it did not exhibit submesoscale features. Results showed that the simulations at 3.5 and 1.2 km resolution allowed the development of submesoscale motions, such as eddies of size 5-20 km and thin filaments of ocean tracers. From the first nesting emerged such features, as well as a more stratified upper-ocean layer and a more energetic ocean surface. The Rossby number distribution showed an effective increase of ageostrophic motions with the increase of horizontal resolution, demonstrating that the transition to submesoscale regime already happens at 3.5 km resolution. Submesoscale motions got more important at 1.2 km resolution, as much larger Rossby number were observed (>10), that were not permitted at the first nesting. At the same time, however, this high resolution led to the development of strong numerical noises that could result in spurious submesoscale motions, as the fluctuating KE spectra of NEST96 for small wavelengths is suggesting. These numerical problems can be solved with sensitivity experiments for the viscosity and the diffusivity coefficients. The difference in the vorticity fields is more striking between the GOFS16 and the NEST32 experiments, than between the NEST32 and the NEST96 experiments. The NEST96 experiment seems to be more a refined version of the NEST32 rather than showing additional features only permitted at this resolution. Overall, it can be stated that submesoscale motions in the Caribbean Sea are able to develop at 3.5 km resolution, and a further increase in resolution should be done carefully.

2. *How long does it take for the solutions to decorrelate in time?*

   The coherence among the resolutions was high, as the SST field demonstrated, and the dominant mesoscale patterns across all solutions was still visible. Yet, the different solutions did not evolve in the same way or at the same rate. As the time-evolution of the mean surface relative vorticity exposed, submesoscale permitting simulations showed a clear departure from the parent model. The adaptation to the new grid was shown by a sudden increase in vorticity (both positive and negative). It took around 6 days for the first nesting to find stability, and around 3 days for the second nesting. The three solutions diverged in this context, but it is hard to tell if they were actually uncorrelated. The decorrelation between the solutions was more clearly demonstrated in the time-evolution of the

SSH maximum of the anticyclonic eddy centre. The increase in horizontal resolution, allowing smaller features to develop, led to the subsiding of eddy centre, and there was a small indication for slowing down the eddy propagation speed. The solution of the first nesting departed from its parent model after 5 days of simulation. From that point, the trends were similar (both increasing), but the solutions were always separated by 1-2 cm. In the case of the second nesting, the solution with its parent model (second nesting) diverged after 4 days of simulation. After that day, the SSH maximum was continuously decreasing, showing opposite trend to the two other simulations. To summarize, the decorrelation among the solutions occurs on a time-scale of days.

3. *Which mechanisms generate the submesoscale motions?*

   Results showed that an increase in horizontal resolution led to the emergence of submesoscale features in the oceanic flow, such as submesoscale eddies of size 5-20 km. Tracers properties were found to be highly dependent on the resolution, as filaments of tracers were getting thinner and concentration higher, as observed in Brannigan et al., 2017. Large temperature and density gradients are indicative of frontogenesis activity, a key element of the upper-ocean submesoscale transition (Capet et al., 2008b). One prominent characteristic of flows with large Rossby number is restratification of the upper-ocean mixed-layer. Such feature emerged in the simulations when comparing the Brunt-Väisälä frequency profile at the three resolutions in a small area of high submesoscale activity. The first 100 m revealed a strong restratification further compensated by a destratification at the ML base. Several authors suggest that this restratification is led by the surface frontogenesis mechanisms triggering divergent motions, which at the same time inhibits the same process to occur at depth, through vertical velocity. In the present simulations, baroclinic instabilities developed as a consequence of density fronts out of geostrophic balance, resulting in submesoscale eddies that further acted to restratify the surface mixed-layer. Whether external forcings or submesoscale eddies are responsible for the upper mixed-layer restratification was not totally clear, since the case study showed that in certain areas, restratification occurred at the mixed-layer base, while a destratification at the surface was caused by the atmospheric forcing. Nevertheless, the high kinetic energy trapped within the upper-ocean layers indicated that the submesoscale motions developed at the surface.

   The filaments were mostly of positive vorticity, perhaps a sign of the dominance of instabilities occurring for $f>0$. The positive skewness could also be explained by the presence of the anticyclonic vortex in the domain. Results from Boccaletti, Ferrari, and Fox-Kemper, 2007 showed that the positive skewness appears as soon as the baroclinic instability enters in the nonlinear stage and continues to grow, which supports the idea that Mixed-Layer Instabilities (MLIs), a common feature in the surface mixed-layer. In our case, the skewness values are rather small, and the positive tail is thick. Even so, the cyclonic vorticity mean is always larger than the anticyclonic mean, arguing for the preponderance of a cyclonic development in the submesoscale, which is expected.

The case study of the shedding of a submesoscale eddy (SME) at the rim of the large anticyclonic eddy demonstrated that the SME arose from the interaction between the oceanic flow and the island, as it occurs in the case of topographic wakes (McWilliams, 2016). At the very location of the SME, large positive Rossby number and large lateral strain rate were observed. Enhanced downward vertical velocity was also observed at this site, which is in accordance with Thomas, Tandon, and Mahadevan, 2008, who mentioned that at sites where lateral strain rate is large, strong ageostrophic overturning circulation generates intense vertical velocities. These vertical velocities usually activate restratification in the ML, but the latter was not observed.

To summarize, in the present study, frontogenesis and topographic wakes have clearly shown to be major initiators of the submesoscale processes.

5.2 Conclusion

Ultimately, it is noteworthy to mention that this dissertation is the result of a first approach to study the submesoscale dynamics in the Caribbean Sea, and that the research has been conducted using data from a short time-period in February 2017. The present study demonstrated that the development of submesoscale motions in the Caribbean sea was made possible at a horizontal resolution of 3.5 km, given that the first internal Rossby radius of deformation is 75 km. High resolution simulations confirmed that submesoscale structures are concentrated in the upper-oceanic layer and are a major component of the surface dynamical modes. Transition to the submesoscale regime happens on a time-scale of days. These small-scale ageostrophic motions, allowed by the new submesoscale-permitting grid, showed significant impact on the mesoscale flow. Their generations were mainly the caused by frontogenesis and topographic wakes. As a result, dynamics in the surface layers involved large Rossby numbers, enhance kinetic energy, and surface restratification. The present study also confirmed that the near-surface dynamics is impacted by an increase in horizontal resolution, while the ocean interior remains in geostrophic balance.

5.3 Future work and outlook

It is important to note that the increase in resolution also brings the emergence of several islands as well as a refined bathymetry and coastlines, all which could also have an impact on the flow structure. For example, the subsiding of the centre of the anticyclonic eddy with an increase in horizontal resolution could be the result of submesoscale vortices at the periphery feeding on the eddy's kinetic energy. This argument is supported by the energy spectra (Fig.4.7) where for an increase in horizontal resolution, the amount of energy stored in smaller scales also increases, diminishing at the same time the energy density at the mesoscales. Likewise, the increase in horizontal resolution also increases the amount of details in the bathymetry, from where islands emerge and the ocean floor becomes more uneven. In shallow regions, like at the site of the anticyclonic eddy, the interaction between the flow and the bathymetry is enhanced, something that could lead to a loss in energy. It is not clear whether the small submesoscale vortices are the main cause for mesoscale eddy to lose energy or if it is exclusively due to the more refined bathymetry. In order to isolate the effects of the bathymetry, one would have to create a simulation in which the horizontal resolution is increasing, but the bathymetry would be kept somewhat constant, by removing some of the emerging islands for example.

It was shown in this thesis that submesoscale motions are confined in the upper-ocean, and have a significant impact on the mesoscale flow. A question that arises is whether submesoscale dynamics have an impact on the transport of ocean tracers. This was studied by Smith, Hamlington, and Fox-Kemper, 2015 and Smith, 2017 for idealized cases, where they showed that turbulent stirring in the submesoscale range affects the heterogeneity in spatial distributions of ocean tracers such as carbon dioxide, nutrients, plankton, and oil. The Caribbean Sea being an important region for phytoplankton blooms (Fig5.1), it would be interesting to study how does the increase in horizontal resolution impact the transport of passive and active tracers.

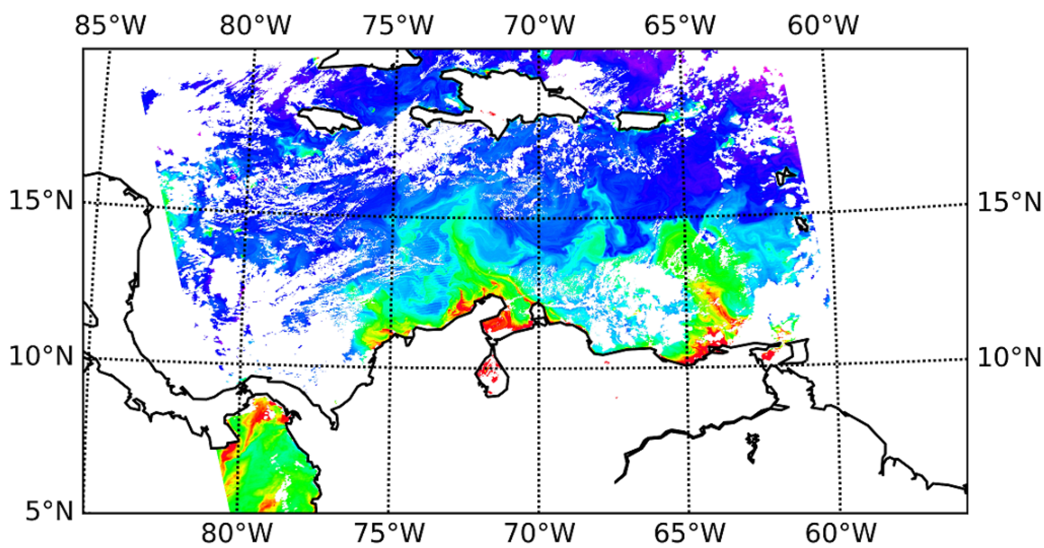

FIGURE 5.1: Chlorophyll-a concentration (mg m^3) on a logarithmic scale in the Caribbean Sea, on Feb. 13th, 2017, from NASA ocean color satellite data.

Bibliography

Andrade, Carlos Alberto, Eric Desmond Barton, and Christopher N. K. Mooers (2003). "Evidence for an eastward flow along the Central and South American Caribbean Coast". In: *Journal of Geophysical Research* 108. DOI: 10.1029/2002JC001549.

Boccaletti, Giulio, Raffaele Ferrari, and Baylor Fox-Kemper (2007). "Mixed Layer Instabilities and Restratification". In: *Journal of Physical Oceanography* 37, pp. 2228–2250. DOI: 10.1175/JPO3101.1.

Brannigan, Liam et al. (2017). "Submesoscale Instabilities in Mesoscale Eddies". In: *Journal of Physical Oceanography* 47, pp. 3061–3085. DOI: 10.1175/JPO-D-16-0178.1.

Capet, X. et al. (2008a). "Mesoscale to Submesoscale Transition in the California Current System. Part I: Flow Structure, Eddy Flux, and Observational Tests". In: *Journal of Physical Oceanography* 36, pp. 29–43. DOI: 10.1175/2007JPO3671.1.

— (2008b). "Mesoscale to Submesoscale Transition in the California Current System. Part II: Frontal Processes". In: *Journal of Physical Oceanography* 36, pp. 44–64. DOI: 0.1175/2007JPO3672.1.

— (2008c). "Mesoscale to Submesoscale Transition in the California Current System. Part III: Energy Balance and Flux". In: *Journal of Physical Oceanography* 38, pp. 2256–2269. DOI: 10.1175/2008JPO3810.1.

Charney, Jule G. (1971). In: *Journal of the Atmospheric Sciences* 28, pp. 1087–1095. URL: 10.1175/1520-0469(1971)028<1087:GT>2.0.CO;2.

Chelton, Dudley B. et al. (1998). "Geographical Variability of the First Baroclinic Rossby Radius of Deformation". In: *Journal of Physical Oceanography* 28, pp. 433–460. URL: 10.1175/1520-0485(1998)028<0433:GVOTFB>2.0.CO;2.

Cushman-Roisin, Benoit and Jean-Marie Beckers (2011). *Introduction to geophysical fluid dynamics: physical and numerical aspects*. Academic press.

Fratantoni, D. M. (2001). "North atlantic circulation during the 1990's observed with satellite-tracked drifters". In: *Journal of Geophysical Research* 106, pp. 22067–22093.

Gordon, Arnold L. (1967). "Circulation of the Caribbean Sea". In: *Journal of Geophysical Research* 72. DOI: 10.1029/JZ072i024p06207.

Gula, J. et al. (2014). *Submesoscale instabilities on the Gulf Stream North Wall In Preparation*. URL: http://stockage.univ-brest.fr/~gula/northwall.html.

Gyory, Joanna, Arthur J. Mariano, and Edward H. Ryan. *The Caribbean Current. Ocean Surface Currents.*

Hernández-Guerra, Alonso and Terrence M. Joyce (2000). "Water masses and circulation in the surface layers of the Caribbean at 66 W". In: *Geophysical Research Letters* 27, pp. 3497–3500.

Iovino, Dorotearico et al. (2016). "A $1/16^\circ$eddying simulation of the global NEMO sea-ice-ocean system". In: *Geosci. Model Dev.* 9, pp. 2665–2684. DOI: 10.5194/gmd-9-2665-2016.

Johns, Williams E. et al. (2002). "On the Atlantic inflow to the Caribbean Sea". In: *Deep Sea Research Part I Oceanographic Research Papers* 49, pp. 211–243. DOI: 10.1016/S0967-0637(01)00041-3.

Jouanno, Julien et al. (2008). "The mesoscale variability in the Caribbean Sea. Part I: Simulations and characteristics with an embedded model". In: *Ocean Modelling* 23, pp. 82–101. DOI: 10.1016/j.ocemod.2008.04.002.

Klein, Patrice et al. (2007). "Upper Ocean Turbulence from High-Resolution 3D Simulations". In: *Journal of Physical Oceanography* 38, 1748—1763. DOI: 10.1175/2007JPO3773.1.

Legg, Sonya and James C. McWilliams (2001). "Convective modifications of a geostrophic eddy field". In: *Journal of Physical Oceanography* 31, pp. 874–891. DOI: 10.1175/1520-0485(2001)031<0874:CMOAGE>2.0.CO;2.

Lévy, Marina et al. (2012). "Bringing physics to life at the submesoscale". In: *Geophysical Research Letters* 39. DOI: 10.1029/2012GL052756.

Madec, G. and the NEMO team (2008). *NEMO ocean engine*. Institut Pierre-Simon Laplace (IPSL), France, No 27: Note du Pôle de modélisation.

Mahadevan, Amala and Amit Tandon (2006). "An analysis of mechanisms for submesoscale vertical motion at ocean fronts". In: *Ocean Modelling* 14, pp. 241–256. DOI: 10.1016/j.oceamod.2006.05.006.

McWilliams, James C. (2016). "Submesoscale currents in the ocean". In: *Proceedings Royal Society A* 472. DOI: 10.1098/rspa.2016.0117.

McWilliams, James C., M. J. Molemaker, and I. Yavneh (2001). "From stirring to mixing of momentum: Cascades from balanced flows to dissipation". In: *Proceedings of the 12th 'Aha Huliko'a Hawai- ian Winter Workshop*, pp. 59–66.

Molemaker, M. J., J. C. McWilliams, and I. Yavneh (2005). "Baroclinic instability and loss of balance". In: *Journal of Physical Oceanography* 35, pp. 1505–1517. DOI: doi.org/10.1175/JPO2770.1.

Nürnberg, Dirk et al. (2002). *R/V SONNE Cruise Report: Rapid Climate Changes in the Western Tropical Atlantic - Assessment of the biogenous and sedimentary record*. GEOMAR, Kiel, Germany.

Olbers, Dirk, Jürgen Willebrand, and Carsten Eden (2012). *Ocean Dynamics*. Springer.

Rayner, N. A. et al. (1966). "Global analyses of sea surface temperature, sea ice, and night marine air temperature since the late nineteenth century". In: *Journal of Geophysical Research* 108, p. 4407. DOI: 10.1029/2002JD002670.

Smith, Katherine M. (2017). "Effects of Submesoscale Turbulence on Reactive Tracers in the Upper Ocean". PhD thesis. University of Colorado.

Smith, Katherine M., Peter E. Hamlington, and Baylor Fox-Kemper (2015). “Effects of submesoscale turbulence on ocean tracers”. In: *Journal of Geophysical Research: Oceans* 121, pp. 908–933. DOI: 10.1002/2015JC011089.

Stone, Peter H. (1966). “On non-geostrophic baroclinic stability”. In: *Journal of the Atmospheric Sciences* 23, pp. 390–400. DOI: 10.1175/1520-0469(1966)023<0390:ONGBS>2.0.CO;2.

Talley, Lynne et al. (2011). *Descriptive Physical Oceanography. An Introduction. 6th edition*. London, UK: Elsevier Ltd.

Thomas, Leif N. and C. M. Lee (2005). “Intensification of ocean fronts by down-front winds”. In: *Journal of Physical Oceanography* 35, 1086—1102. DOI: 10.1175/JPO2737.1.

Thomas, Leif N., Amit Tandon, and Amala Mahadevan (2008). “Submesoscale Processes and Dynamics”. In: *Geophysical Monograph Series* 117, 17—38. DOI: 10.1029/177GM04.

Trotta, Francesco et al. (2016). “A Structured and Unstructured grid Relocatable ocean platform for Forecasting (SURF)”. In: *Deep-Sea Research II* 133, 54—75. DOI: 10.1016/j.dsr2.2016.05.004.

Trotta, Francesco et al. (2017). “Multi-nest high-resolution model of submesoscale circulation features in the Gulf of Taranto”. In: *Ocean Dynamics* 67, 1609—1625. DOI: 10.1007/s10236-017-1110-z.